Influence of storm timing and forward speed on tides and storm surge during Hurricane Matthew

Ajimon Thomas[a,*], JC Dietrich[a], TG Asher[b], M Bell[c], BO Blanton[d], JH Copeland[c], AT Cox[e], CN Dawson[f], JG Fleming[g], RA Luettich[b]

[a] Dept. of Civil, Construction, and Environmental Engineering, North Carolina State University, 2501 Stinson Drive, Raleigh, NC 27607, United States of America
[b] Institute of Marine Sciences, University of North Carolina, 150 Coker Hall, 3431 Arendell St., Morehead City, NC 28557, United States of America
[c] WeatherFlow Inc., 320 East Vine Drive, Fort Collins, CO 80524, United States of America
[d] Renaissance Computing Institute, 100 Europa Drive, Suite 540, Chapel Hill, NC 27517, United States of America
[e] Oceanweather Inc., 350 Bedford Street, Suite 404, Stamford, CT 06901, United States of America
[f] Institute of Computational Engineering and Sciences, The University of Texas at Austin, Austin, TX 78712, United States of America
[g] Seahorse Coastal Consulting, 3103 Mandy Lane, Morehead City, NC 28557, United States of America

ARTICLE INFO

Keywords:
ADCIRC
SWAN
Inundation
Hindcasting
HSOFS mesh
OWI wind fields

ABSTRACT

The amount and extent of coastal flooding caused by hurricanes can be sensitive to the timing or speed of the storm. For storms moving parallel to the coast, the hazards can be stretched over a larger area. Hurricane Matthew was a powerful storm that impacted the southeastern U.S. during October 2016, moving mostly parallel to the coastline from Florida through North Carolina. In this study, three sources for atmospheric forcing are considered for a simulation of Matthew's water levels, which are validated against extensive observations, and then the storm's effects are explored on this long coastline. It is hypothesized that the spatial variability of Matthew's effects on total water levels is partly due to the surge interacting nonlinearly with tides. By changing the time of occurrence of the storm, differences in storm surge are observed in different regions due to the storm coinciding with other periods in the tidal cycles. These differences are found to be as large as 1 m and comparable to the tidal amplitude. A change in forward speed of the storm also should alter its associated flooding due to differences in the duration over which the storm impacts the coastal waters. With respect to the forward speed, the present study contributes to established results by considering the scenario of a shore-parallel hurricane. A faster storm caused an increase in peak water levels along the coast but a decrease in the overall volume of inundation. On the other hand, a slower storm pushed more water into the estuaries and bays and flooded a larger section of the coast. Implications for short-term forecasting and long-term design studies for storms moving parallel to long coastlines are discussed herein.

1. Introduction

Matthew was a tropical cyclone that reached Category-5 hurricane status on the Saffir-Simpson hurricane wind scale during 2016. Matthew affected about 1900 km of coastline in the United States, caused 34 direct deaths and forced evacuations by 3 million people (Stewart, 2017). Between 1900 UTC 06 October when the storm was located offshore of Miami, Florida, and 0600 UTC 09 October when it was located offshore of Cape Hatteras, North Carolina, Matthew remained close to the coast and moved along a shore-parallel track (Fig. 1) with a relatively-slow forward speed of 5 to 7 m/s. Observations indicate large variations in peak water levels all along the U.S. Atlantic coast, and we hypothesize that this was caused by the storm's slower forward speed and shore-parallel track, which allowed it to interact with different stages in the tidal cycle at different locations and over several days.

Several studies have examined the interactions between tides and surge. In the 1950s, Proudman developed theoretical solutions for the propagation of an externally forced tide and surge into an estuary of uniform section (Proudman, 1955, 1957) and also identified the tendency of peak surge to most often occur on high tides, which was later confirmed (Prandle and Wolf, 1978; Rossiter, 1961). Tides and surge can also interact nonlinearly, thus causing the water levels to be even higher or lower than their individual contributions would suggest, due to feedbacks through bottom friction, shallow-water effects, and advection (Wolf, 1978). Nonlinear parameterization of bottom stress was

* Corresponding author.
E-mail addresses: athomas9@ncsu.edu (A. Thomas), jcdietrich@ncsu.edu (J. Dietrich).

https://doi.org/10.1016/j.ocemod.2019.03.004
Received 30 July 2018; Received in revised form 18 December 2018; Accepted 3 March 2019
Available online 08 March 2019

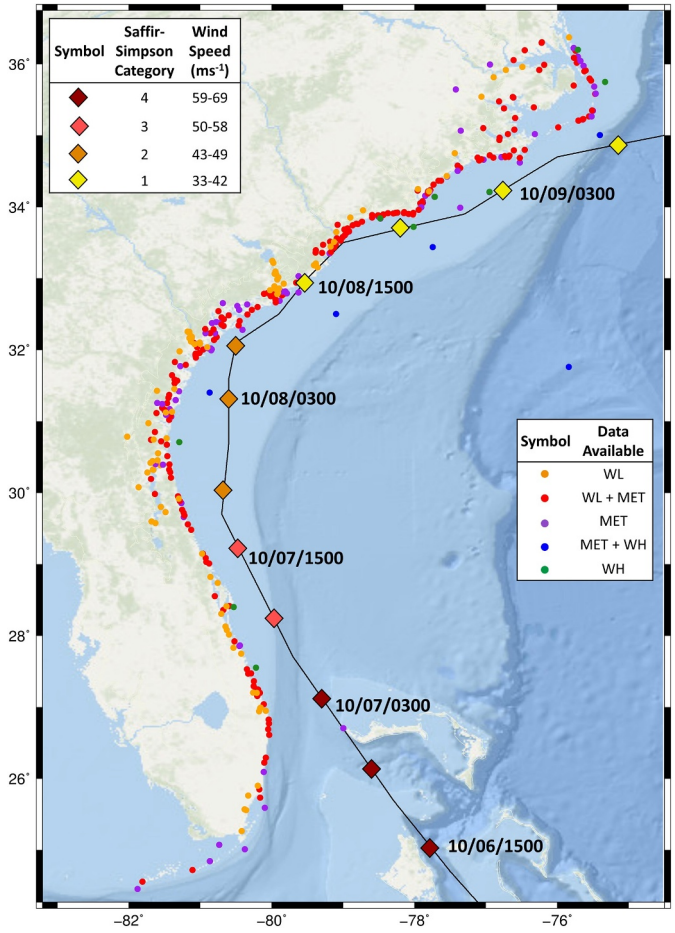

Fig. 1. NHC best track for Matthew (black line and diamonds), along with observation locations (circles) on the U.S. southeast coast. High-water marks are not shown. The storm center positions are shown every 6hrh and color-coded to categories on the Saffir-Simpson scale. The storm positions are labeled in dates/times relative to UTC. The observation locations are color-coded to indicate whether they have data for meteorology (MET), waves (WH), and/or water levels (WL).

found to the primary contributor to nonlinear tide-surge interactions along the Queensland coast of Australia (Tang et al., 1996), on the east coast of Canada and northeastern United States (Bernier and Thompson, 2007), and along the Fujian coast (Zhang et al., 2010). Along the southeast coast of the United States, Coriolis acceleration was found to be a significant contributing factor to these perturbations (Feng et al., 2016; Valle-Levinson et al., 2013). The magnitude of these interactions can be large, reaching as high as 70% of the tidal amplitudes (Rego and Li, 2010) along the Louisiana-Texas coast during Hurricane Rita, and 74 cm (Idier et al., 2012) for storms in the English Channel. The tide-surge nonlinearities were also large with a mean absolute value of 60% of the tide magnitude (Lin et al., 2012) for synthetic surge events in New York Harbor, and at least 15–20% for idealized cyclone tracks and straight coastlines representing the west coast of India (Poulose et al., 2017).

It can be challenging to include these nonlinear interactions in surge predictions. Flood risk studies typically represent the hurricane climate by using the Joint Probability Method (JPM) with synthetic storms to determine the flooding at various return periods. The effect of tides can be a crucial factor in these studies. For studies looking at smaller regions with small and in-phase tidal amplitudes, tides were introduced as a constant addition to the JPM integral error term (Niedoroda et al., 2010). Other studies included tides into the JPM analysis by randomly adding tidal heights to the surge response (Blanton et al., 2012; Ho and Myers, 1975; U.S. Army Corps of Engineers, 2018b). However, these additions do not incorporate the often-large effect of the nonlinear interactions between the surge and tides. The present study quantifies these interactions along the entire U.S. southeast coast during Matthew, including their variation from the continental shelf into the estuaries. The representation of coastal floodplains is larger than in previous studies and can allow the flooding from the shore-parallel storm to interact with multiple phases of the tides.

The effects of storm parameters like size, landfall location, wind speeds, and direction of approach on surge have also been studied previously (Irish et al., 2008; Sebastian et al., 2014; Weisburg and Zheng, 2006). The effect of storm forward speed can vary. The surge can be greater for a faster storm, e.g., for a standard hurricane on a representative shelf (Jelesnianski, 1972). Along the Louisiana-Texas shelf for Hurricane Rita, increasing the forward speed of the storm caused higher surges but smaller total flooded volumes (Rego and Li, 2009). But the surge and inundation areas can also be greater for a slower storm, e.g., for the estuaries of North Carolina (Peng et al., 2004), and for the Dutch coast (Berg, 2013). For the Charleston Harbor in South Carolina, although a slower storm can produce larger inundation areas, whether or not it can produce larger surge depends on the faster storm's speed and the distance of the track from the harbor (Peng et al., 2006). While these studies have identified the vulnerability of the coastline to hurricane storm surge under different scenarios, they considered small regions or idealized coastlines, and storms that moved perpendicular to the coastline. The present study uses Hurricane Matthew's track along the coast from Florida to North Carolina to examine how the forward speed of a shore-parallel storm affects the surge and inundation along a complex estuarine coastline and coastal floodplain.

This study uses the coupled ADCIRC + SWAN model, which has proven to be accurate in flood predictions in many coastal systems (Dietrich et al., 2018; Hope et al., 2013; Suh et al., 2015). The model utilizes an unstructured, finite-element mesh developed for surge and tide predictions for the U.S. Atlantic and Gulf coasts (Riverside Technology and AECOM, 2015). The unstructured mesh can represent a large domain, while using sufficient resolution to represent the complex shoreline. This combination allows for comprehensive validation and scenario testing. The goals of this study are to better understand the influence of storm timing and forward speed on flooding for a shore-parallel storm in a large domain. The goals are addressed by (a) validating model predictions of winds, and water levels during Matthew on a mesh with floodplain coverage over a large extent, (b) quantifying the contributions of nonlinear interactions to the total water levels, and (c) quantifying the differences in flooding due to differences in the storm's forward speed and time relative to the tidal cycle.

2. Hurricane Matthew

2.1. Synoptic history

Matthew began as a tropical wave off the west coast of Africa on 23 September 2016 (Stewart, 2017), and by 1200 UTC 28 September, measurements indicated a tropical storm formation about 27 km west-northwest of Barbados. Moving into the Caribbean Sea, Matthew attained hurricane status on 1800 UTC 29 September about 300 km northeast of Curaçao. Matthew then turned west-southwest and intensified to an estimated peak intensity of 75 m/s(Category-5) on 0000 UTC 1 October. Over the next few days, the storm weakened to a Category-4 status as it moved northward and made landfall with peak wind speeds of 66 m/s over Haiti (1100 UTC 4 October) and 59 m/s over Cuba (0000 UTC 5 October). By 1200 UTC 6 October, the storm brought hurricane-force winds and flooding rains to most of the central and northwestern Bahamas with a peak wind speed of 64 m/s. The Category-4 hurricane made landfall near West End, Grand Bahama Island, around 0000 UTC 7 October (Stewart, 2017).

A broad eastward-moving mid-latitude trough located over the

central United States then caused Matthew to turn toward the north-northwest (Stewart, 2017) and impact much of the southeastern U.S. (Fig. 1). The storm weakened to a Category-3 hurricane around 0600 UTC 7 October about 64 km east of Vero Beach, Florida, and to a Category-2 hurricane by 0000 UTC 8 October about 92 km east-northeast of Jacksonville Beach, Florida. As the storm moved northward, its wind field expanded causing hurricane-force wind gusts across the coastal regions of southeastern Georgia and southern South Carolina. The mid-latitude trough then caused the storm to weaken to a Category-1 status (Stewart, 2017). Moving nearly parallel to the coast of South Carolina, Matthew made landfall around 1500 UTC 8 October just south of McClellanville, South Carolina. The center of the hurricane then traveled offshore of the coast of South Carolina and remained just offshore of the coast of North Carolina through 9 October. Contributions from Matthew's tropical moisture, the ongoing extratropical transition and an increasing pressure gradient from an approaching cold front caused sustained hurricane-force winds over the Outer Banks and significant sound-side storm-surge flooding during the early hours of 9 October. Matthew lost its tropical characteristics by 1200 UTC 9 October, as it moved away from the U.S. (Stewart, 2017).

2.2. Extensive observations along U.S. East Coast

Matthew's effects on surface pressures and wind speeds, offshore and nearshore waves, and coastal water levels are well-described by observational data. Along the southeastern U.S. coast from Florida through North Carolina (Fig. 1), the National Oceanic and Atmospheric Administration (NOAA), the U.S. Geological Survey (USGS), and other agencies collected information at hundreds of buoys, permanent and rapidly deployed gauges and stations, and real-time sensors. Along the storm's path, surface pressures were observed at 283 locations, wind speeds and directions were observed at 66 locations, and significant wave heights were observed at 16 locations (Table 1). Time series observations at buoys and stations operated by the NOAA National Data Buoy Center (NDBC) and the NOAA National Ocean Service (NOS) show how the peak, 10-minute-averaged wind speeds evolved during the course of the storm. Wave parameters were also observed at many of these same locations.

These winds and waves caused setup and storm surge along the southeastern U.S. coastline. NOS and USGS permanent and rapidly-deployed gauges collected observations; time series of water levels at 501 locations and 612 high-water marks (HWMs) were identified within the model extent. For the analyses herein, observations were omitted that did not operate during the storm peak or that showed elevated water levels after the storm due to freshwater run-off or wave run-up, thus leaving 289 time series and 464 HWMs to describe storm surge (Table 1). These observations are used to validate our predictive models for winds, and storm surge.

3. Methods

Predictions of waves and storm surge are sensitive to the atmospheric conditions used as forcing to the model simulations. In this study, we evaluate forcings from three sources: a vortex model based on storm parameters like the track, forward speed, and isotach radii; and two data-assimilated products available after the storm. Then the most-accurate atmospheric forcing is used for a detailed hindcast of Matthew's effects on water levels throughout the southeastern U.S., via comparison with extensive observations. This study uses the depth-averaged, barotropic version of ADCIRC, because the strong surface stresses during storms causes the water column to be well-mixed in shallow nearshore and coastal regions. This hindcast is then used as the basis for studies of the nonlinear interactions between tides and surge, and of the effects of storm timing and forward speed. In this section, details are provided about the three sources for surface pressure and wind fields that were evaluated for hindcasts of Matthew, as well as the input settings for the coupled ADCIRC + SWAN model.

3.1. Surface pressure and wind fields

Hydrodynamic predictions are analyzed with three sources of atmospheric forcing: a parameterized vortex model based on storm parameters from the National Hurricane Center (NHC), and two data-assimilated products. For all three sources, the surface pressures and wind velocities are developed (either by the parametric model or by interpolation from the data-assimilated products) at the computational points in the model domain. ADCIRC accounts for canopy cover and applies a surface roughness reduction factor increases to full marine winds as overland regions are inundated (Kerr et al., 2013).

3.1.1. Parametric vortex model

It is common to use parametric vortex models to represent storm wind fields based on limited input information (Hu et al., 2012, 2015; Xie et al., 2006). These models assume a hyperbolic radial pressure field that depends on the ambient and cyclone central surface pressures, the radius to maximum winds, and the hurricane-shape parameter (Holland, 1980; Schloemer, 1954). Several parametric vortex models have been used within ADCIRC to generate wind and pressure fields in forecasting applications (Dietrich et al., 2013a; Mattocks and Forbes, 2008; Mattocks et al., 2006). The most complete is the Generalized Asymmetric Holland Model (GAHM), which has been shown to be a better representation than earlier versions (Gao et al., 2017), and to

Table 1
Numbers of available observations for atmospheric, wave, and water-level responses to Matthew.

Data source	Reference	Surface pressure	Wind speed	Wind direction	Significant wave height	Water levels	High water marks
NOS	National Oceanic and Atmospheric Administration (2018b)	19	19	19		21	
NDBC	National Oceanic and Atmospheric Administration (2017)	15	15	15	7		
CORMP	University of North Carolina Wilmington (2018)	6	6	6	3		
NERRS	National Oceanic and Atmospheric Administration (2018c)	5	5	5			
USACE	U.S. Army Corps of Engineers (2018a)				1		
UNC CSI	University of North Carolina (2018)				1		
CDIP	Scripps Institution of Oceanography (2018)				4		
ICON	National Oceanic and Atmospheric Administration (2018d)	3	3	3			
ENP	National Park Service (2018)		1	1			
FIT	Florida Institute of Technology (2018)	1	1	1			
USGS-PERM	U.S. Geological Survey (2018b)					77	
USGS-DEPL	U.S. Geological Survey (2018c)	8	6	7		17	464
USGS-STS	U.S. Geological Survey (2018c)	210				168	
NCEM	North Carolina Emergency Management (2018)	10	10	10		6	
TOTAL		277	66	67	16	289	464

compare well with observation-based analysis products and full-physics numerical models (Cyriac et al., 2018; Dietrich et al., 2018). In this study, GAHM is used with the NHC Best Track storm parameters for Matthew (Stewart, 2017) to generate surface pressures and wind speeds at every computational point in the ADCIRC domain. Unlike the two atmospheric forcings described below, GAHM is not data-assimilated and only represents the vortex, with no far-field m eteorological representation.

3.1.2. Data-assimilated atmospheric products

Surface pressure and wind velocities from WeatherFlow Inc. (WF) were developed using the Weather Research and Forecasting (WRF) model (Skamarock et al., 2008), which can simulate weather processes at synoptic scales down to large eddy simulations at microscales. During Matthew, 52 stations measured sustained wind speeds greater than 22 m/s, with 32 stations measuring gusts of at least 33 m/s. These observations were assimilated into fields of surface pressures and wind velocities. These fields cover a period from 2000 UTC 06 October 2016 until 2000 UTC 09 October 2016, at 10-min intervals. The fields cover from latitude 24.15°N to 38.67°N and from longitude 83.55°W to 72.02°W with square elements of 96.12 arc-seconds (approximately 3 km north–south by 3 km east–west). The surface pressures and wind velocities are interpolated in space and time to the ADCIRC computational points within the WF domain (Fig. 2).

The second source for data-assimilated products was Oceanweather Inc. (OWI), whose fields are based on observations from anemometers, airborne and land-based Doppler radar, airborne stepped-frequency microwave radiometer, buoys, ships, aircraft, coastal stations and satellite measurements (Bunya et al., 2010). For Matthew, the Tropical PBL (TropPBL) model (Cardone et al., 1994; Thompson and Cardone, 1996) was applied in the core during the entire storm, with hand analysis overlay from 2100 UTC 06 October 2016 until 1500 UTC 09 October 2016, to better represent the interaction of the storm with the coast. The resultant wind and pressure fields are then subject to manual kinematic analysis using the IOKA system to add features that are not well-resolved by the TropPBL model, as well as in-situ, satellite, and aircraft data, into the final fields. These fields represent 30-min sustained wind velocities at a reference height of 10 m above the ground/sea level with consideration to marine exposure. Lagrangian-based interpolation is then used to produce fields at 15 min intervals. For use as atmospheric forcing to hydrodynamic models, the surface pressure and wind fields are represented with a lower-resolution basin grid and a higher-resolution region grid (Fig. 2). The basin grid covers from latitude 5°N to 42°N and from longitude 99°W to 55°W with a spatial resolution of 0.25°, whereas the higher-resolution region field covers from latitude 15°N to 40°N and from longitude 82°W to 68°W with a spatial resolution of 0.05°, both covering a period from 0000 UTC 01 October 2016 until 0000 UTC 11 October 2016, at 15 min intervals.

3.2. Coupled models for nearshore waves and circulation

The storm-induced waves and circulation during Matthew must be predicted by models that can represent their interactions over a wide range of temporal and spatial scales, including coastal flooding into overland regions. We use the coupled SWAN + ADCIRC models (Dietrich et al., 2012, 2011b), which have been validated extensively for flooding during tropical cyclones (Bhaskaran et al., 2013; Dietrich et al., 2018; Hope et al., 2013; Suh et al., 2015).

The unstructured-mesh version of SWAN uses a sweeping Gauss-Seidel method to propagate efficiently the wave action density (Booij et al., 1999; Zijlema, 2010). The action balance equation is used to incorporate source/sink terms for nearshore wave physics, such as triad nonlinear interactions, bottom friction and depth-limited breaking, in addition to deep-water physics of quadruplet nonlinear interactions and whitecapping. The simulations in this study use SWAN version 41.01 with a time step of 600 s. The spectral space is discretized using 36 directional bins with directional resolution of 10° and 40 frequency bins with a logarithmic resolution over the range 0.031 to 1.42 Hz. This logarithmic discretization of frequencies is based on the ratio of $\Delta f/f = 0.1$ for the discrete interaction approximation of the quadruplet

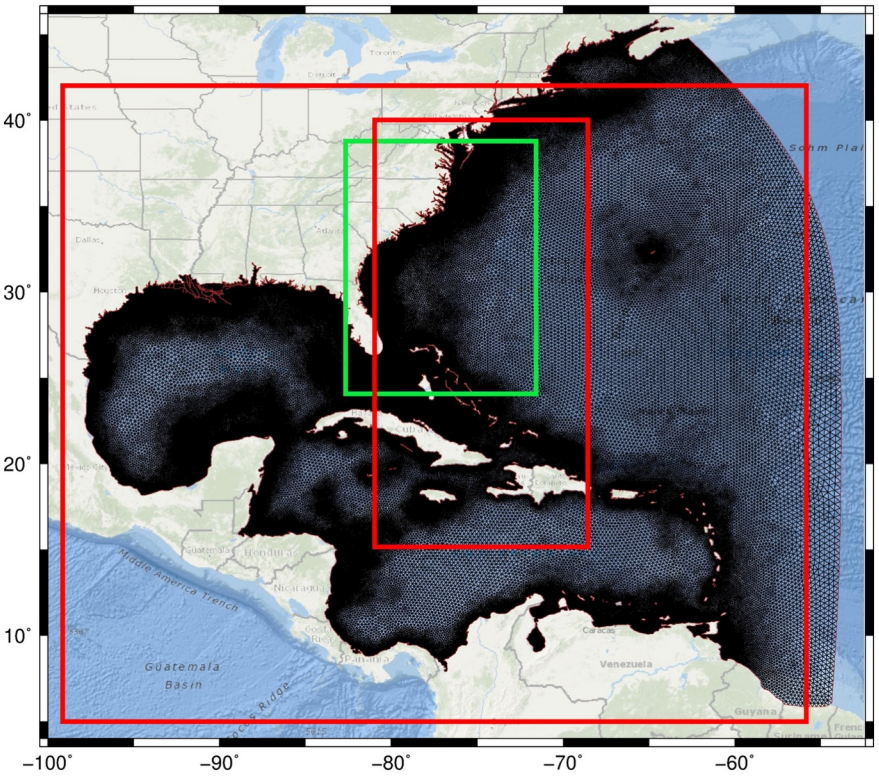

Fig. 2. Coverage area of the WF (green) and OWI (red) wind grids over the HSOFS unstructured mesh (black).

interactions (Hasselmann et al., 1985). This spectral discretization and other physical and numerical settings are the same as used in previous hindcast studies by the authors (Dietrich et al., 2011a, 2013b). To prevent excessive directional turning or frequency shifting at a single vertex due to steep gradients in bathymetry or ambient currents, the spectral velocities in SWAN are limited using a CFL restriction (Dietrich et al., 2013b) with an upper limit of 0.25.

ADCIRC uses the continuous-Galerkin finite element method to solve the shallow water equations on unstructured meshes (Dawson et al., 2006; Kolar et al., 1994; Luettich and Westerink, 2004; Luettich et al., 1992; Westerink et al., 2008). Water levels are calculated using the Generalized Wave Continuity Equation (GWCE), which is a combined and differentiated form of the continuity and momentum equations (Kinnmark, 1986), whereas depth-averaged current velocities are determined from the vertically-integrated momentum equations. For the simulations in this study, ADCIRC version 52.30.13 is used in explicit mode with the lumped mass matrix form of the GWCE (Tanaka et al., 2011). The bottom drag is applied using a depth-dependent quadratic friction law, with a drag coefficient set by the Manning's n value specified for every vertex (Luettich and Westerink, 2004; Luettich et al., 1992). These Manning's n values are also used by SWAN to compute roughness lengths based on the updated ADCIRC water levels at each mesh vertex (Bretschneider et al., 1986; Dietrich et al., 2011a; Madsen et al., 1988). The minimum bathymetric height and friction-surface velocity required for wetting are 0.10 m and 0.01 m/s, respectively. The spatially-constant horizontal eddy viscosity for the momentum equations was set to 50 $m^2 s^{-1}$, and an ADCIRC time step of 1 s was used. The wind drag coefficients on the water surface are calculated using the Garratt formulation (Garratt, 1977; Westerink et al., 2008) with an upper limit of $C_D = 0.002$, similar to previous studies (Dietrich et al., 2012, 2011a). The advective transport terms were enabled to account for nonlinear interactions between surge and tides.

The unstructured-mesh spectral wave model SWAN and the shallow water circulation model ADCIRC were integrated into a coupled SWAN + ADCIRC model so they share the same computational cores and the same unstructured mesh (Dietrich et al., 2012, 2011b). ADCIRC interpolates the wind velocities and computes water levels and velocities, and then supplies them to SWAN, which uses them in its computations for evolution of spectral action density. At the end of each SWAN time step, wave radiation stresses and their gradients are computed by SWAN, and then passed on to ADCIRC, which applies them as surface stresses in its momentum equations. The coupling interval is taken to be the same as the SWAN time step of 10 min.

3.3. Unstructured mesh to describe the southeast U.S. coast

This study uses the Hurricane Surge On-Demand Forecasting System (HSOFS) mesh, which provides coverage of nearshore regions and coastal floodplains along the entire U.S. coast from Texas through Maine (Riverside Technology and AECOM, 2015). The widespread coverage of the HSOFS mesh is possible because its local mesh resolution is typically coarser than meshes for specific coastal regions. The mesh has an average resolution of 500 m along the coast with some areas decreasing to a resolution of 150 m. At most locations, the mesh extends inland to a smoothed version of the 10-m topographic contour (Fig. 3). It has a total of 1,813,443 vertices and 3,564,104 elements. Two primary data sources were used to provide bathymetry/topography: the USGS 1/9 arc second National Elevation Dataset (NED) Digital Elevation Model (DEM) (U.S. Geological Survey, 2018a) supplied overland topography and the NOAA East Coast 2012 (EC2012) tidal constituent database mesh (Szpilka et al., 2016) supplied bathymetry. The mesh has been validated for 10 major tropical and extra-tropical storms covering a spectrum of landfalls across the U.S. coast including Isabel, Katrina, Ike, and Sandy (Riverside Technology and AECOM, 2015). The HSOFS mesh is ideal for this study because its widespread coverage includes the nearshore regions and floodplains impacted by Matthew along the southeast U.S. coast.

3.4. Adjustments for water level processes on longer time scales

To represent baroclinic and longer-term processes, water levels were adjusted *a priori* to account for local sea level rise and intra-annual mean sea surface variability. These adjustments are provided as a spatially-varying offset surface, and are thus an improvement over the spatially-constant adjustments used in previous studies (e.g., Bunya et al., 2010; Dietrich et al., 2018, 2011a). They provide a correction to the mean water levels before the storm, without the expense of running a three-dimensional, baroclinic model from the open ocean into the floodplains.

The ground elevations in the HSOFS mesh are referenced to local mean sea level based on the National Tidal Data Epoch from 1983 through 2001, and thus the sea level must be adjusted to conditions during Matthew in 2016. Sea level trends were computed at 29 NOAA tidal stations extending from Florida through Maine, using relationships provided by the NOAA Center for Operational and Oceanographic Products and Services (CO-OPS) (National Oceanic and Atmospheric Administration, 2018a) for a 15-year period from 2001 to 2016, to account for local increases in mean sea level relative to the datum used by the HSOFS mesh. This increase ranges from 3 to 5 cm for much of Florida through South Carolina, but increases to 7 to 8 cm in northeast North Carolina and Virginia (Fig. 4).

The water levels were also adjusted to account for steric effects due to thermal expansion of the ocean waters (Antonov et al., 2005; Levitus et al., 2000; Willis et al., 2004) and baroclinic interactions with the Gulf Stream (Ezer et al., 2013) using the regional long-term sea level station data at the time of landfall (Bunya et al., 2010). For Matthew, the steric adjustment resulted in a maximum water level increase of about 19 cm along the Georgia coast, but decreases to about 10 cm to the south in Florida and to the north in North Carolina and Virginia (Fig. 4).

The total vertical reference level adjustment at each station was calculated as the sum of the local sea level rise and steric increase. This increase was then applied as an offset surface, which varies spatially along the coast, and transitions offshore to zero. This offset surface was provided to ADCIRC at the start of the simulation using a 1-day ramp and is implemented as a pseudo-barometric pressure term in ADCIRC (Asher et al., 2019).

4. Model validation

Hindcasts of Matthew were simulated with SWAN + ADCIRC and atmospheric forcing from the three sources: GAHM, WF, and OWI. To establish the ambient water level condition prior to the storm, the tides were spun-up in a 15-day simulation from 0000 UTC 17 September to 0000 UTC 02 October. Then the storm was simulated over a 9-day period from 0000 UTC 02 October to 0000 UTC 11 October.

4.1. Atmospheric forcings

4.1.1. Evolution of surface pressures and wind speeds

The observed and predicted surface pressures and wind speeds are compared at selected locations ranging from Florida through North Carolina (Fig. 5) and throughout the storm's evolution (Figs. 6–7). Surface pressures are analyzed as pressure deficits, where an ambient pressure of 1013.25 hPa is subtracted from observed and predicted pressures. On 0800 UTC 07 October, when the storm was located offshore of Melbourne, Florida (Fig. 6, first row), north-northeasterly winds were observed at the NDBC station TRDF1 at Trident Pier, Florida, with a maximum wind speed of 22.9 m/s and a pressure deficit of about 40 hPa (Fig. 7, first row). GAHM over-predicts the peak wind speeds by about 10 m/s and under-predicts the pressure deficit by 20 hPa.

On 2000 UTC 07 October (about 10 h later, and 19 h before

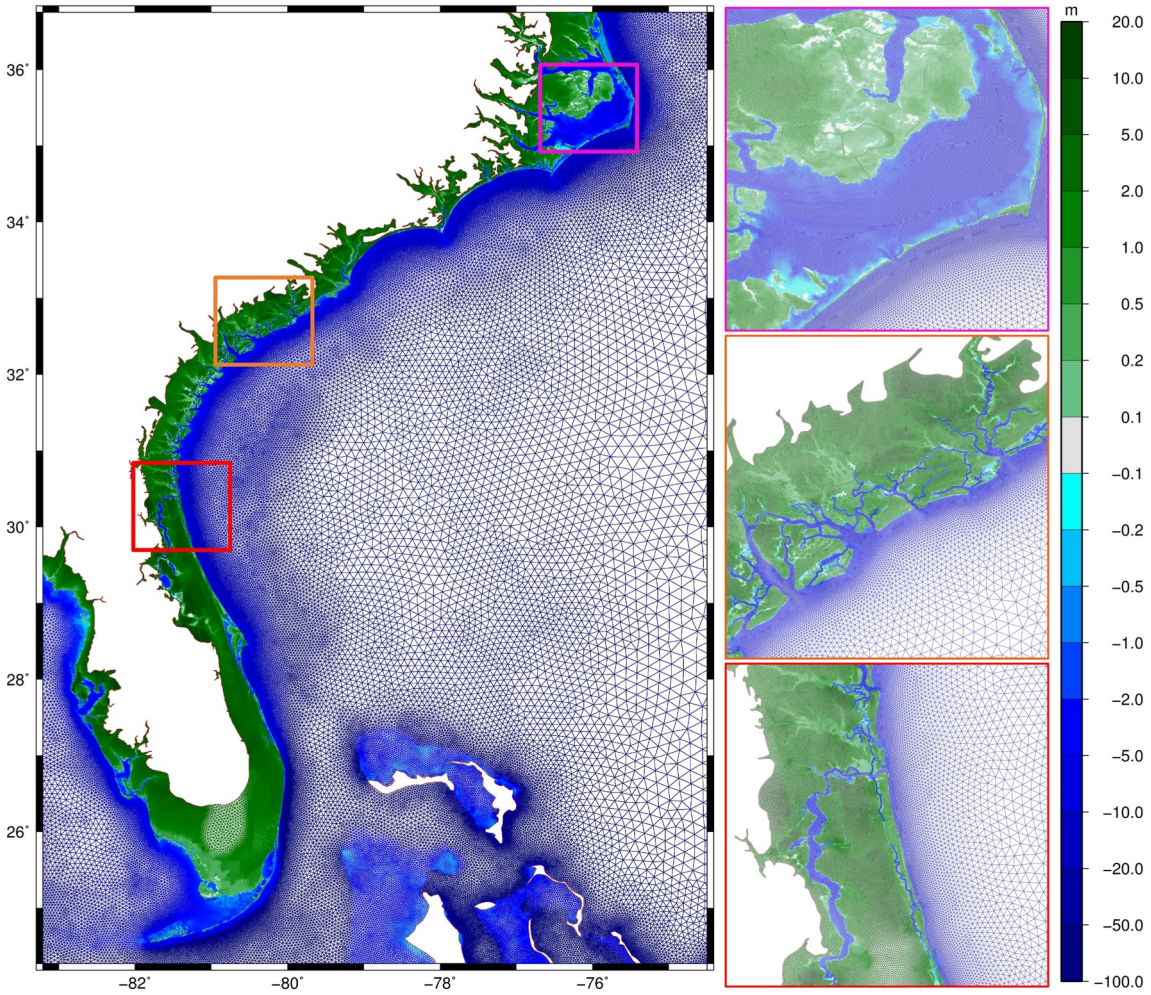

Fig. 3. The HSOFS mesh topography and bathymetry (m relative to LMSL), contoured on the mesh elements (left figure). Colored boxes indicate specific regions as shown on the right: The Pamlico Sound, North Carolina (pink), the Cooper and Savannah Rivers along the South Carolina-Georgia coast (orange) and Upper Florida showing the Fernandina Beach and St. Johns River (red).

landfall), when the storm was located 35 miles east of St. Augustine, Florida (Fig. 6, second row), the wind speeds decreased in all three fields. Close to the eye, the winds interact with the coast, with peak wind speeds of 25 to 30 m/s for both GAHM and OWI, and 20 m/s for WF. At this time, the NOS station MYPFI located at the entrance of the St. Johns River, Florida, received north-northeasterly winds with a maximum wind speed of 22.7 m/s and pressure deficit of about 28 hPa (Fig. 7, second row). As Matthew moved northward, it brought hurricane-strength wind gusts to the coasts of southeastern Georgia and southern South Carolina. On 0615 UTC 08 October (about 9 h before landfall), the USGS station 311941081265201 near Brunswick, Georgia, recorded a maximum wind speed of 16.1 m/s and a pressure deficit of about 29 hPa (Fig. 7, third row), with all the three atmospheric forcings having similar results.

When the storm reached offshore of Charleston, South Carolina, it had weakened to Category-1 status. On 1350 UTC 08 October (about 1 h before landfall), the offshore NDBC buoy 41004 observed southwesterly winds with a maximum speed of 23.5 m/s and a pressure deficit of 31.55 hPa (Fig. 7, fourth row). At the peak, all three models gave similar results, except for GAHM under-predicting the pressure deficit by about 20 hPa. On 1500 UTC 08 October, the Category-1 storm made landfall in McClellanville, South Carolina (Fig. 6, third row) with observed wind speeds of 39 m/s (Stewart, 2017). Near landfall, there is a difference in the storm track, with both GAHM and OWI predicting a slight inland trajectory for the storm compared to WF. After landfall, the storm moved offshore in an east-northeastward direction.

By 0600 UTC 09 October, the storm was located 45 km offshore of Cape Hatteras, North Carolina (Fig. 6, bottom row). The eye of the storm is similar for GAHM and OWI with a large eye surrounded by a small 10 to 15 m/s wind field, although GAHM has a much larger 25 to 30 m/s field offshore. At the NDBC buoy 41025 at Diamond Shoals, wind speeds at this time were 18 m/s, which matches for WF and OWI. The eye for WF has become disorganized and extends into Pamlico Sound. There are significant differences inside the sound, with modeled winds in the ranges of 20 to 30 m/s, 5 to 15 m/s, and 10 to 20 m/s for GAHM, WF, and OWI, respectively. The effects of Matthew's wind field were observed even at the NOS station 8652587 located north at the Oregon Inlet Marina, North Carolina, where a maximum wind speed of 20.56 m/s and a pressure deficit of about 20 hPa was recorded on 1006 UTC 9 October (Fig. 7, last row). The storm weakened to a tropical depression by 1200 UTC 9 October, when it was located 45 km southeast of Cape Hatteras.

Overall, for the surface pressures (Fig. 7, left column), GAHM tends to under-predict the pressure deficits during the storm by more than 10 hPa. But the central pressure comes from the best-track file and represents an input to the GAHM, which is then used to produce the surface barometric field. Thus, these under-predictions are almost entirely a result of errors in the central pressure coming from the best-track file. The data-assimilated WF and OWI products show a good match to the surface pressures at most locations, with exceptions of: WF before and after the storm, due to its relatively shorter time period; and OWI at NOS station BFTN7 at Beaufort, North Carolina, where it under-

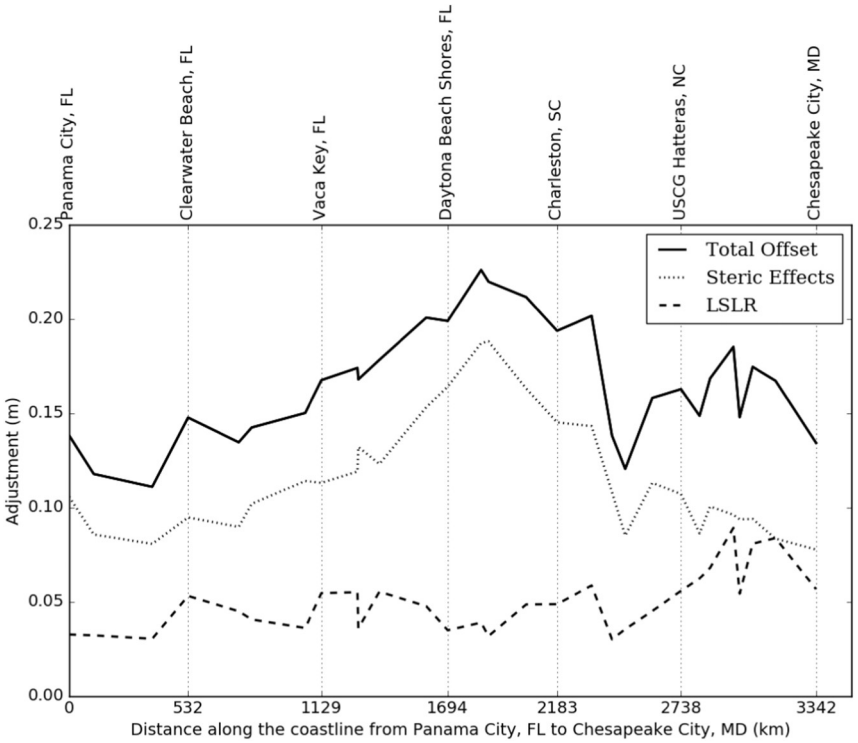

Fig. 4. Variation of offset values (m) along the U.S. southeast coast. Adjustments are shown for local sea level rise (dashed), steric effects (dotted), and total offset (solid).

predicted the pressure deficit during the storm. The peak wind speeds are also matched well between observations and predictions (Fig. 7, right column). The parametric GAHM has zero wind speeds before and after the storm, and it also tends to over-predict the peaks at locations in Florida (TRDF1) and into the Carolinas (41024, BFTN7). The data-assimilated WF and OWI products capture the large-scale synoptic wind patterns as well as the storm winds.

4.1.2. Error statistics

The agreement between observations and predictions is quantified (Table 2) through the use of the root-mean-squared error E_{RMS}:

$$E_{RMS} = \sqrt{\frac{1}{N}\sum_{i=1}^{N} E_i^2}$$

and the mean normalized bias B_{MN}:

$$B_{MN} = \frac{\frac{1}{N}\sum_{i=1}^{N} E_i}{\frac{1}{N}\sum_{i=1}^{N} |O_i|}$$

where N is the number of observations and E_i is the difference between predicted and observed values. The E_{RMS} is an indication of the magnitude of error and has an ideal value of zero. The B_{MN} indicates the model's magnitude of over-prediction or under-prediction normalized to the observed value and also has an ideal value of zero. For surface pressures and wind speeds, as well as for water levels in the upcoming sections, these error statistics are calculated for a period ranging from 0000 UTC 05 October to 0000 UTC 11 October.

GAHM has the largest E_{RMS} and magnitude of B_{MN}, thus showing the benefits of the data-assimilated WF and OWI products. Both GAHM and WF under-predict the surface pressure deficits with negative B_{MN} values of -0.16 and -0.02, respectively, whereas OWI over-predicts the surface pressure deficit with a positive B_{MN} of 0.06. Although the peak wind fields in GAHM were the strongest (Fig. 6), the negative B_{MN} reflects GAHM's lack of ambient winds before and after the storm. WF and OWI have positive B_{MN} for wind speeds of 0.16 and 0.06, respectively, thus indicating over-prediction. For both surface pressure deficits and wind speeds, OWI has smaller errors overall, and thus it is the best match to the observations.

Thus, OWI is a better representation of the atmospheric forcing during Matthew. It is a better match to the observed time series of surface pressures and wind speeds, at locations throughout the region (Table 2). Its fields also show the most-realistic representation of the storm's evolution near landfall and afterward (Fig. 6). In the following sections, the authors will use OWI as the best approximation of the true behavior of Matthew as it moved offshore of the U.S. southeast coast. Although error statistics will be computed for water levels as forced with all three atmospheric sources, only OWI will be used in the analyses of spatial and temporal variability of storm surge, and only OWI will be used in the analyses of nonlinear interactions, storm timing and forward speed.

4.2. Water levels

4.2.1. Evolution of water levels

As Matthew tracked along the southeast coastline of the United States, heavy winds and rainfall elevated water levels at several locations to historic levels. Although Matthew brought northerly and northeasterly hurricane peak winds of 20 to 25 m/s along the Florida coast from Lake Worth to Port Canaveral, it resulted in very little storm tide with a maximum of 0.5 to 1 m (Fig. 8, top left). As the storm moved northward, there was an increase in the water levels along the coastline. On 1700 UTC 07 October (Fig. 8, top right), winds blowing from the northeast pushed water against the coastline with peaks of 1.5 to 2.5 m. The USGS-STS stations FLVOL03143 and FLSTJ03126 located between Orlando Beach and St. Augustine Beach, Florida, recorded peak water levels of 2.1 m and 2.56 m, respectively (Fig. 9, top row). The winds decreased as the storm moved northward and weakened from Category-3 to Category-2 status. The station NOS 8720218 at Mayport, Florida and located at the entrance of the St. Johns River, received peak winds of 20 to 25 m/s, causing a maximum water level of

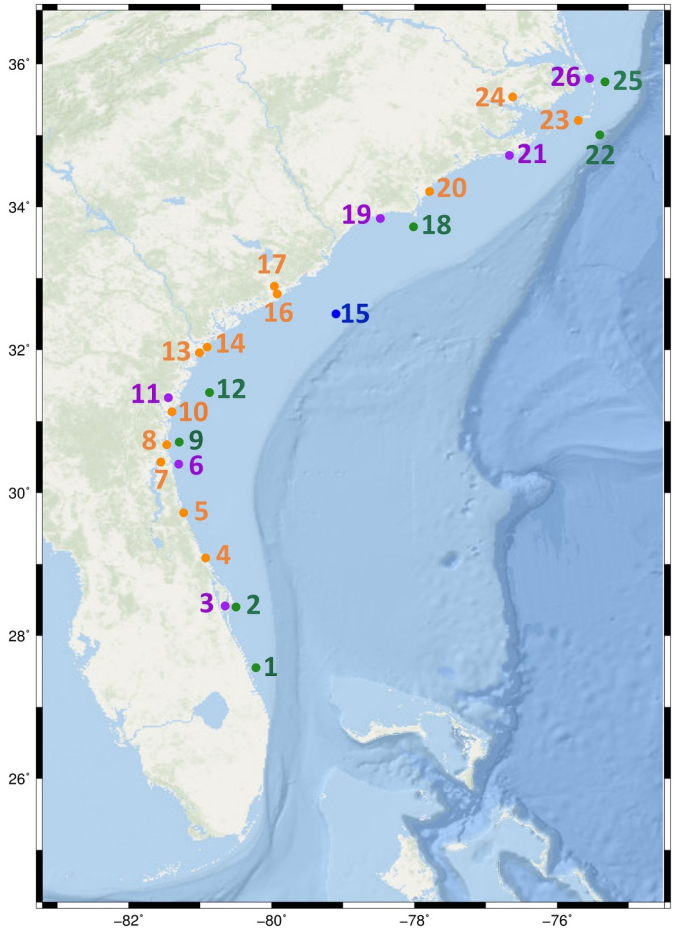

Fig. 5. Locations of selected stations for comparison of surface pressures, wind speeds, significant wave heights and water levels. The points are color coded as in Fig. 1 and numbered from south to north.

1.59 m, the highest ever recorded at this site (Stewart, 2017) (Fig. 9).

Along the St. Johns River, inundation occurred well inland from the coast (Fig. 8, top right). The NOS 8720625 station at Racy Point observed a record peak of 1.58 m on 2236 UTC 07 October (Stewart, 2017), about 3.5 h after a maximum was observed at the river entrance. North of the St. Johns River along the Florida Coast, Matthew caused storm tides of 2 to 2.3 m. On 0200 UTC 08 October (Fig. 8, center left), the storm now centered offshore of Georgia, caused shore-parallel winds to drive water levels of 1 to 1.5 m into the relatively deep tidal inlets and sounds that separate the barrier islands stretching 160 km between the St. Mary's and Savannah Rivers. Stations along the rivers that extend from these sounds recorded even higher peaks. The USGS-PERM 02226180 and USGS-STS GACHA17861 measured peak water levels of 1.87 m and 2.30 m, respectively (Fig. 9, third row).

On 0800 UTC 08 October (Fig. 8, center right), approximately 7 h before landfall, easterly and north-easterly winds pushed water into the Savannah River, causing water levels larger than 2.5 m. The maximum storm surge recorded by a tide gauge in the United States during Matthew was at NOS 8670870 (Fig. 9), located at the entrance of the Savannah River, where peak surge occurred during high-tide and caused maximum water levels of 2.59 m. As Matthew moved northward, a combination of wind and storm surge caused extensive damage along the South Carolina coastline. The USGS-STS sites on the islands south and east of Beaufort County, South Carolina, recorded peaks of 2 to 2.5 m. The highest peak of all observations collected during Matthew was at the USGS-STS SCBEA14284 at Bluffton, southwest of Beaufort, where a maximum of 2.66 m was recorded. As a Category-1 storm, Matthew caused extensive flooding in Charleston, South Carolina. At the tidal gauge NOS 8665530 (Fig. 9) located at the Cooper River Entrance, a peak surge occurred during a low-tide resulting in a storm tide maximum of 1.87 m. On 1500 UTC 08 October at landfall (Fig. 8, bottom left), south-easterly winds pushed water levels of 1.5 to 2 m against the coastline from Bulls Bay to Myrtle Beach.

The maximum water levels in North Carolina varied significantly by location. For the Atlantic coastline south of Oak Island, the maximum water levels were mostly in the range of 2 to 2.5 m. This decreased to 1.5 to 2 m from Oak Island to Masonboro Inlet and 1 to 1.5 m for the coastline from Wrightsville Beach to Cape Hatteras. On 0600 UTC 09 October (Fig. 8, bottom right), northerly and northeasterly winds pushed water levels of 0.5 to 1 m toward the western Pamlico Sound. The NOS 8654467 gauge at the United States Coast Guard station on Hatteras Island, received record water levels (Stewart, 2017) with a peak of 1.85 m (Fig. 9, bottom left). On the rivers that drain into the Sound, the maximum water levels varied in the range of 0.5 to 1 m in the Neuse River, and 0.75 to 1.25 m in the Pamlico and Pungo Rivers (e.g., NCEM BLHN7 in Fig. 9, bottom right). As the storm moved offshore, the winds decreased along the coast, and the water levels returned to normal tide levels at most locations.

4.2.2. *Error statistics*

At most locations, the SWAN + ADCIRC predictions (with OWI atmospheric forcing) show good agreement with the observations (e.g., the 12 stations shown in Fig. 5 with time series in Fig. 9). One exception was NOS 8654467, where the model underestimated the peak by more than 0.5 m. There was an over-prediction of the peak at some stations (USGS-STS FLVOL03143, NOS 8720218, USGS-PERM02226180 and USGS-STS GACHA17861), but within 0.3 m. Otherwise, the model was able to closely predict variations in both the tides and surge levels. To quantify the model performance with regard to water level predictions, error statistics were computed (Table 2) only at locations wetted by the model. For 241 locations on the U.S. southeast coast, the overall E_{RMS} was 0.28 m and the B_{MN} was very close to zero. The largest errors occurred on the gauges upstream of the Savannah River, where E_{RMS} of about 0.58 to 1.27 m and B_{MN} of 0.83 to 1.56 were obtained. Large E_{RMS} of 0.41 to 0.94 m and B_{MN} of −0.56 to −0.87 were also observed at stations on the Sound side of the Outer Banks in North Carolina. These over-predictions in the Savannah River and under-predictions in the North Carolina Sounds can likely be attributed to the relatively-coarse representation of the channels and tidal inlets that lead to these locations. Comparing the overall statistics for water levels, simulations with GAHM had the highest E_{RMS} of 0.42 m and B_{MN} of − 0.32, while simulations with OWI had the smallest E_{RMS} of 0.28 m and B_{MN} of 0.04. Simulations with GAHM and WF had negative B_{MN} and thus under-predicted the water levels.

A total of 464 USGS-observed HWMs inside the model domain were found to be suitable for analysis. When combined with the 289 hydrograph-derived peak water levels, a total of 753 locations were used to evaluate model performance during Matthew along the U.S. southeast coast. In Fig. 10, the points are color-coded based on error (predicted less observed) expressed as percentage of the observed value. Warm colors indicate regions of over-prediction by ADCIRC, whereas cooler colors indicate regions of under-prediction. For the simulation forced by OWI, the errors in modeled peaks were within 10% at 322 (52%) of the 622 total stations wetted by ADCIRC and within 25% at 538 (87%) stations. For the scatter plots, the R^2 value was 0.78 and the slope of the best-fit line was 0.96 (Table 2). The E_{RMS} were largest on the Sound side of the Outer Banks in North Carolina. The model under-predicted the peaks by more than 25% at most locations in this region. In other regions, the errors were lesser especially along the coast from Florida to South Carolina, where the errors were usually less than 25%. A negative value of B_{MN} indicated an under-prediction of the peaks overall by all the three models. As seen for water levels, the observation-based OWI and WF fields led to better error statistics than GAHM for the predicted water levels. The best correlation between modeled

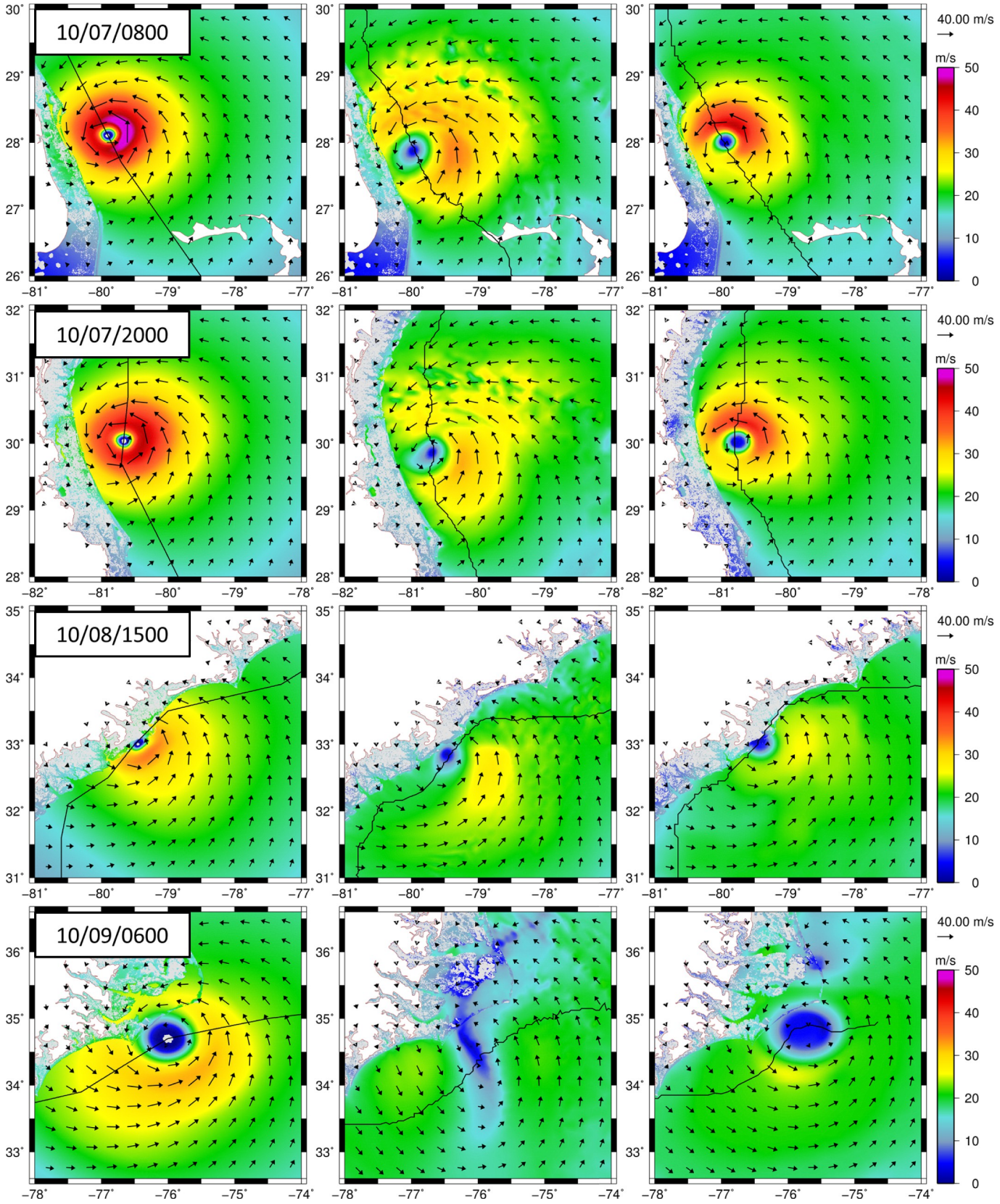

Fig. 6. Hindcasts of wind speeds (m/s) during Matthew along the U.S. southeast coast. Rows correspond to: (top) 0800 UTC 07 October, approximately 31 h before landfall; (second from top) 2000 UTC 07 October, approximately 19 h before landfall; (second from bottom) 1500 UTC 08 October, approximately at landfall; and (bottom) 0600 UTC 09 October, approximately 15 h after landfall. Columns correspond to: (left) GAHM; (center) WF; and (right) OWI. Black lines represent the storm track for each source.

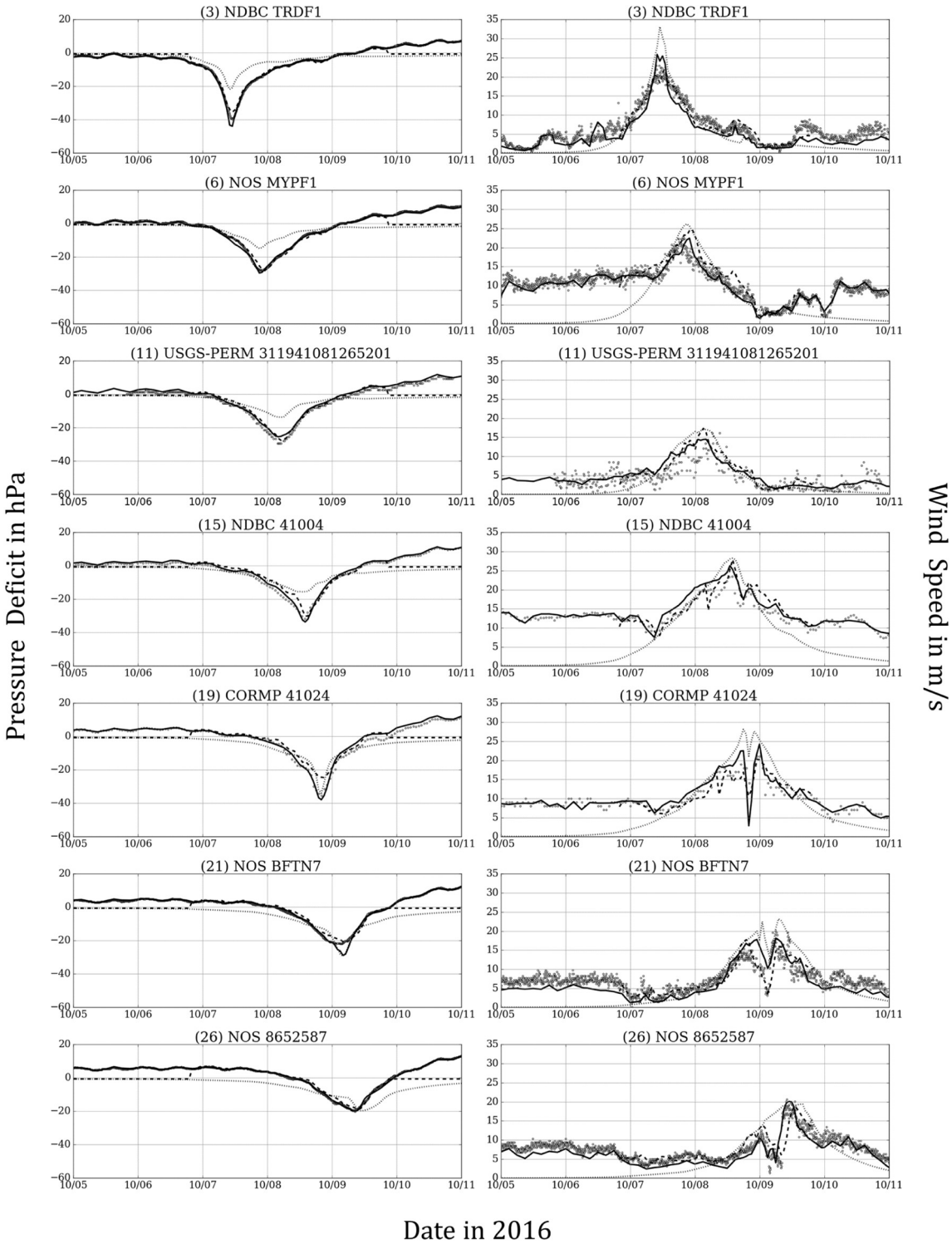

Fig. 7. Time series of pressure deficits in hPa (left column) and wind speeds in m/s (right column) at seven locations (rows) shown in Fig. 5. Observed values are shown with gray circles and predicted results using lines: GAHM (dotted), WF (dashed) and OWI (solid).

and observed peaks were given by OWI with its better values of E_{RMS}, B_{MN}, R^2 and best-fit slope.

Thus, the SWAN + ADCIRC simulation on the HSOFS mesh with OWI atmospheric forcing is the best prediction of the surface pressures, wind speeds, and water levels along Matthew's track from Florida through North Carolina. The water levels are a good match at both open-coast and inland locations, and the error statistics are comparable to other recent studies with SWAN + ADCIRC on higher-resolution meshes (e.g., Hope et al., 2013). It is noted that the simulation was not tuned to achieve this performance; the mesh and other input settings are similar to other studies, including real-time forecasting with ADCIRC. Using this well-validated simulation, we can now quantify the contributions of the nonlinear terms in ADCIRC, and then investigate the effects of storm timing and forward speed on the peak water levels.

Table 2
Error statistics for surface pressure deficits, wind speeds, water levels, and high water marks.

Parameter	Error	Model GAHM	WF	OWI
Surface pressure deficit	Stations	283	283	283
	E_{RMS} (hPa)	6.72	4.23	2.14
	B_{MN}	−0.16	−0.02	0.06
Wind speed	Stations	66	61	66
	E_{RMS} (m/s)	5.60	2.98	2.29
	B_{MN}	−0.29	0.16	0.06
Water level	Stations	233	238	241
	E_{RMS} (m)	0.42	0.37	0.28
	B_{MN}	−0.32	−0.27	0.04
High water marks	Stations	613	612	622
	E_{RMS} (m)	0.58	0.48	0.28
	B_{MN}	−0.21	−0.19	−0.03
	R^2	0.51	0.65	0.78
	Best-fit slope	0.78	0.80	0.96

5. Surge interactions with tides, storm timing and forward speed

5.1. Nonlinear tide-surge interaction

The total storm tide should include contributions from both surge and tides. However, instead of a linear superposition, there are physical processes that causes their interaction to be a nonlinear phenomenon (Bernier and Thompson, 2007; Horsburgh and Wilson, 2007; Poulose et al., 2017; Prandle and Wolf, 1978; Tang et al., 1996; Wolf, 1981). These processes are represented in the governing equations in ADCIRC as: (a) momentum advection on the surge due to the presence of the tide; (b) the nonlinear effects of bottom friction due to the quadratic parametrization; (c) the Coriolis acceleration (Feng et al., 2016; Valle-Levinson et al., 2013); and (d) the shallow water effect (Idier et al., 2012; Prandle and Wolf, 1978; Zhang et al., 2010), which arises due to nonlinearities related to $H = h + \zeta$ terms in the mass and momentum equations. The importance of these terms varies from case to case and is associated with water depth, tidal ranges, and storm strength at specific locations. These nonlinear terms influence the distribution of energy between tide and surge and thus can be a crucial factor in the accurate prediction of total water levels during a hurricane. The goal of the present study is not to re-investigate the possible causes of these nonlinear interactions, but rather to quantify their behavior during a shore-parallel storm affecting a long coastline. In contrast to earlier studies in this region (Feng et al., 2016; Valle-Levinson et al., 2013), which used a typical resolution between 1 and 5 km along the coastline, this study includes sufficient resolution to represent the behavior of the interactions into the estuaries and coastal water bodies.

To separate the nonlinear interaction term from the storm tide, the nonlinear term can be computed as $(\eta_I) = (\eta_{T+W}) - (\eta_W + \eta_T)$, where each η represents water levels from a simulation with some combination of winds (W) and/or tides (T) (Bernier and Thompson, 2007; Rego and Li, 2010; Zhang et al., 2010). Therefore, the offset surface was disabled only for this subsection, to exclude the effects of relative sea level rise and steric effects on the nonlinear interaction between tide and surge. It is noted that, because we are using the depth-averaged, barotropic version of ADCIRC, this study may not represent all of the dynamics on the deeper shelf. However, it is a reasonable assumption that the storm's effects were distributed well into the water column, and the computational efficiency of the depth-averaged version allows for additional resolution to explore the interactions into the estuaries and coastal regions.

During Matthew, it was seen that the nonlinear interactions were large especially in regions with broader-shelf areas (Fig. 11). In the estuaries along the South Atlantic Bight, the peak magnitudes of the nonlinear interactions were larger than 1 m. Farther offshore from the estuaries, the maximum values decreased to about 0.1 to 0.4 m along the coastline and to zero in the open-ocean. The tide-surge interaction significantly affected the total water levels only when they were large enough to interact. Our results show that with respect to Local Mean Sea Level (LMSL), the nonlinearities are destructive ($\eta_I < 0$) to the storm tide heights during a rising or high tide, and constructive ($\eta_I > 0$) during a low or falling tide. These results are similar to previous studies (Lin et al., 2012; Rego and Li, 2010). At locations along Blackbeard Creek to the south of Savannah, Georgia (Fig. 12), the interaction terms were small with a maximum of 0.27 m at station 1 located offshore. Moving inland, the magnitudes increased to a maximum of 0.48 m at station 2 near the coast and 1.04 m at station 3 in the estuary. At station 3, the nonlinear terms were as large as the tidal amplitudes. These values are large enough to be of practical importance during storm surge forecasting. There is also a phase shift in the peak of the nonlinear terms as compared to that to the surge, as has been recognized previously (Horsburgh and Wilson, 2007). At station 3, this phase shift was 5 h.

Thus, the tide-surge nonlinear interactions during Matthew occurred on the shallow and wider-shelf regions of the domain and varied in sign based on the tidal cycles. Although similar trends have been seen in the literature, this is the first study to represent the interactions into the estuaries and floodplains over a long coastline for a shore-parallel storm, and with representation of these features at appropriate resolution. The magnitudes of these nonlinear terms were largest in the estuaries along the southeastern U.S. coast and are larger than in any of the previous studies. The nonlinear tide-surge interactions can have a significant effect in controlling the total water levels during a hurricane.

5.2. Storm timing

The total water levels caused by Matthew as it moved along the U.S. coastline were affected by both variations in tidal amplitudes and by its coincidence with different parts of the tidal cycle at different locations. To understand how Matthew's time of occurrence would have influenced the total water levels along the coast, scenarios were simulated to alter the storm's timing relative to the tidal cycle. For the U.S. southeast coast, the dominant tidal constituent is the principal lunar semi-diurnal M_2 tidal constituent. Thus simulations were conducted by delaying the storm by 3.11 h, 6.21 h, 9.32 h and 12.42 h, corresponding to one-fourth, half, three-fourth and full M_2 tidal periods, respectively. The storm forward speed was unchanged during these simulations.

These scenarios resulted in water levels that varied from that during the storm, with the greatest changes occurring during the + 6.21 h simulation and least changes happening during the + 12.42 h simulation. These variations are shown in Fig. 13, where warm colors indicate an increase in water level and cool colors indicate a decrease in water levels. In regions like the Pamlico Sound where tides are small, there were no variations in the scenarios. In regions along the coastline where tides are dominant, the changes were larger and extended into the estuaries along the South Atlantic Bight. These plots indicate how the inundation along the U.S. southeast coastline would have varied if Matthew occurred at a different time.

To understand the changes in flooding at specific locations along the coastline, the maximum water levels during Matthew and the two scenarios above were plotted along the U.S. Atlantic coast (Fig. 14). Near Trident Pier, Florida, where the surge occurred during a falling stage in the tidal cycle during Matthew, all scenarios caused increased flooding, especially the + 6.21 h simulation, which produced an increase of about 0.7 m. Near Fort Pulaski, Georgia, where maximum inundation was observed during Matthew, the surge coincided with a lower high tide. If the storm had been delayed by 12.42 h, then the surge peak would have coincided with a higher high tide, thus further increasing the peak by about 0.20 m. Near Wrightsville Beach, North Carolina, where the surge occurred during a rising stage of the tide

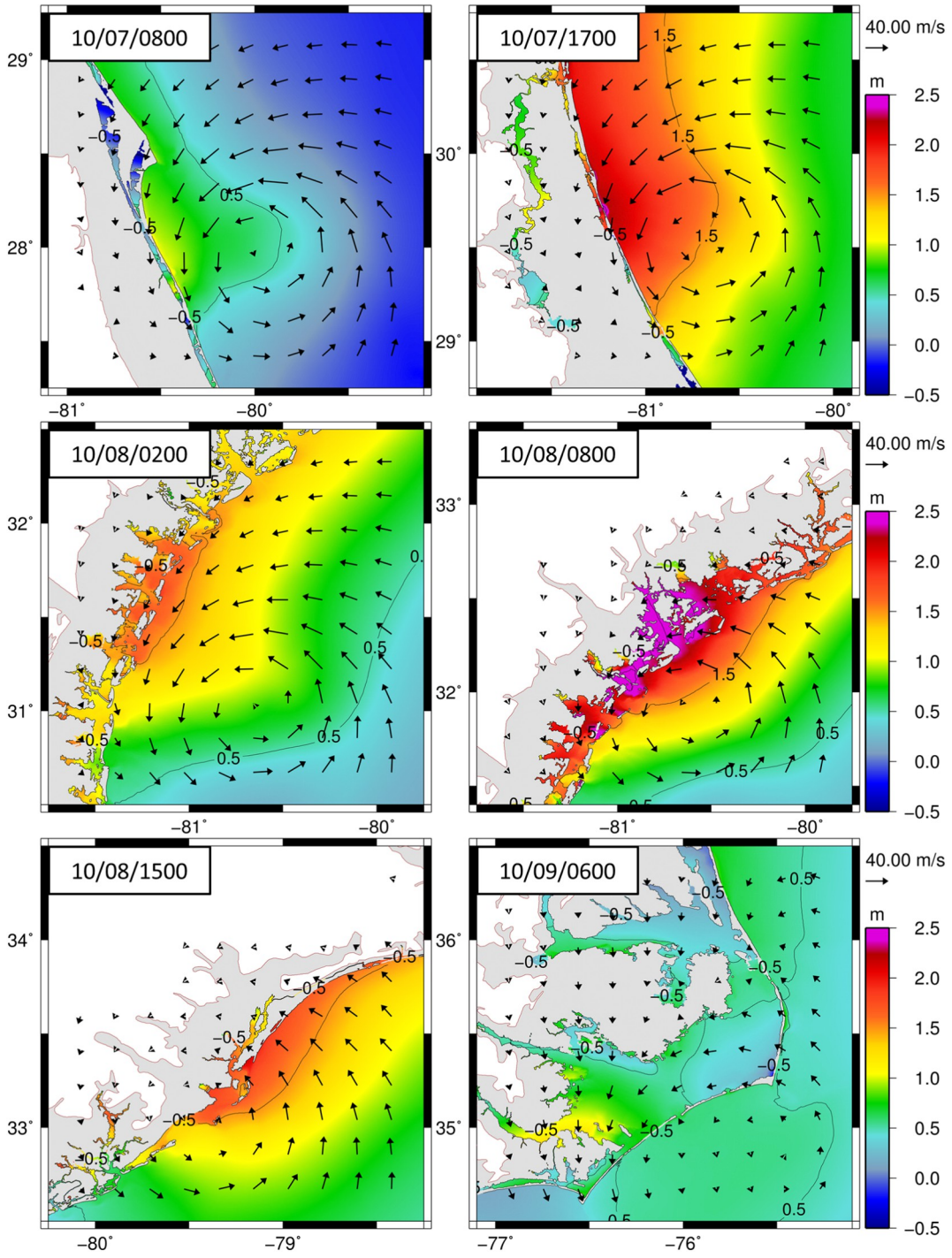

Fig. 8. Contours of water levels (m relative to NAVD88) and vectors of OWI wind speeds (m/s) during Matthew along the U.S. southeast coast. Times correspond to: (top left) 0800 UTC 07 October, approximately 31 h before landfall; (top right) 1700 UTC 07 October, approximately 22 h before landfall; (center left) 0200 UTC 08 October, approximately 13 h before landfall; (center right) 0800 UTC 08 October, approximately 7 h before landfall; (bottom left) 1500 UTC 08 October, approximately during landfall; and (bottom right) 0600 UTC 09 October, approximately 15 h after landfall.

cycle, the peak would have increased by about 0.20 m if the surge had occurred 3.11 h later. Thus, for a shore-parallel storm like Matthew that interacted with tides over a large extent of the coastline, timing can significantly influence the flooding at locations along the coast.

5.3. *Forward speed*

The impact of a hurricane's forward speed on coastal flooding has been recognized previously (Berg, 2013; Jelesnianski, 1972; Peng et al., 2004, 2006; Rego and Li, 2009) and has been shown to have significant effects on peak surge heights and inundation volumes. For a given wind speed, slower storms are generally considered to be more dangerous as they have considerably more time to impact the coastal waters and thus cause more flooding. Matthew had a forward speed of about 5 m/s as it passed North Carolina. In three scenario simulations, the forward speeds were 50% slower, 50% faster and 100% faster, which represent storm speeds of about 2.5 m/s, 7.5 m/s and 10 m/s, respectively, in North Carolina. These speeds are representative of the historical record

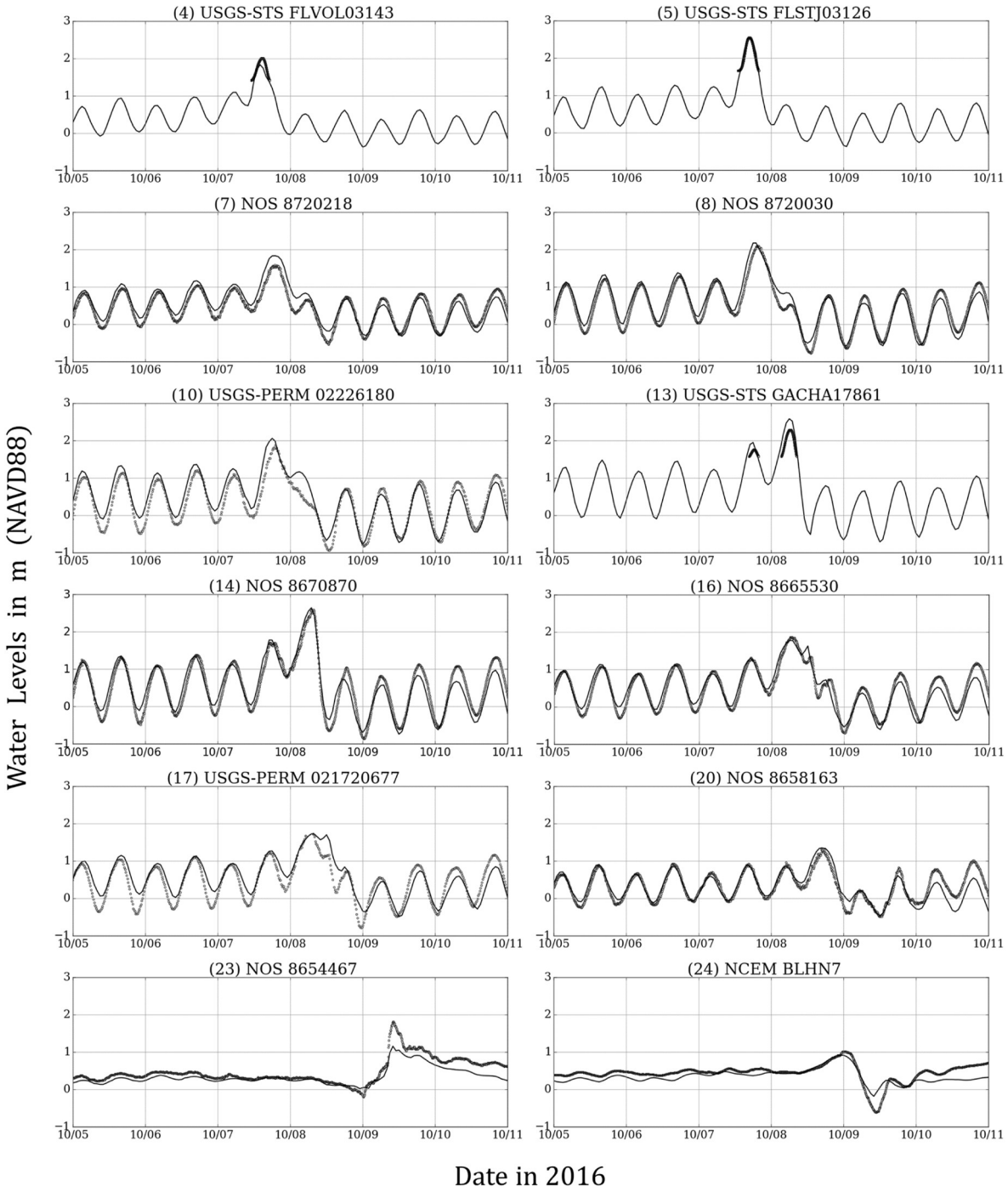

Fig. 9. Time series of water levels (m relative to NAVD88) at 12 locations shown in Fig. 5. Observed values are shown with gray circles, and predicted values using OWI (solid).

(Blanton and Vickery, 2008). Tides were disabled in these simulations, in order to quantify the sole effect of forward speed on surge along this coastline.

The differences in maximum water levels between these scenarios and the base Matthew simulation (Fig. 15) demonstrate how the flooding is affected by the forward speed of the storm. The 50% slower simulation had a decrease in flooding along the open coast. However, with more time to push water into inland areas, the slower storm caused an increase in flooding in the rivers (0.2 to 0.4 m in the St. Johns River, Florida, and Alligator River, North Carolina) and sounds (0.1 to 0.4 m in Pamlico Sound) along the coast. The surge was also higher and pushed further inland in the estuaries and floodplains along the South Atlantic Bight. Near Savannah, Georgia, the water levels increased by about 0.9 m. As the speed of the storm was increased, the trends in water levels were seen to reverse. Water levels were increased on the open coast, but water levels were decreased in the bays and estuaries. The coastline between Daytona Beach and St. Augustine, Florida, had increased flooding of about 0.5 m. Along the coastline of southeast North Carolina, the water levels were also increased by 0.5 m. The increase in water levels along the South Atlantic Bight coastline was lesser and this may be due to the extensive lowlands in the region that absorb more surge. Reduced flooding was observed in the estuaries along the Bight. Near Savannah, Georgia this decrease was as much as 0.7 m.

These trends can be further quantified by examining the maximum

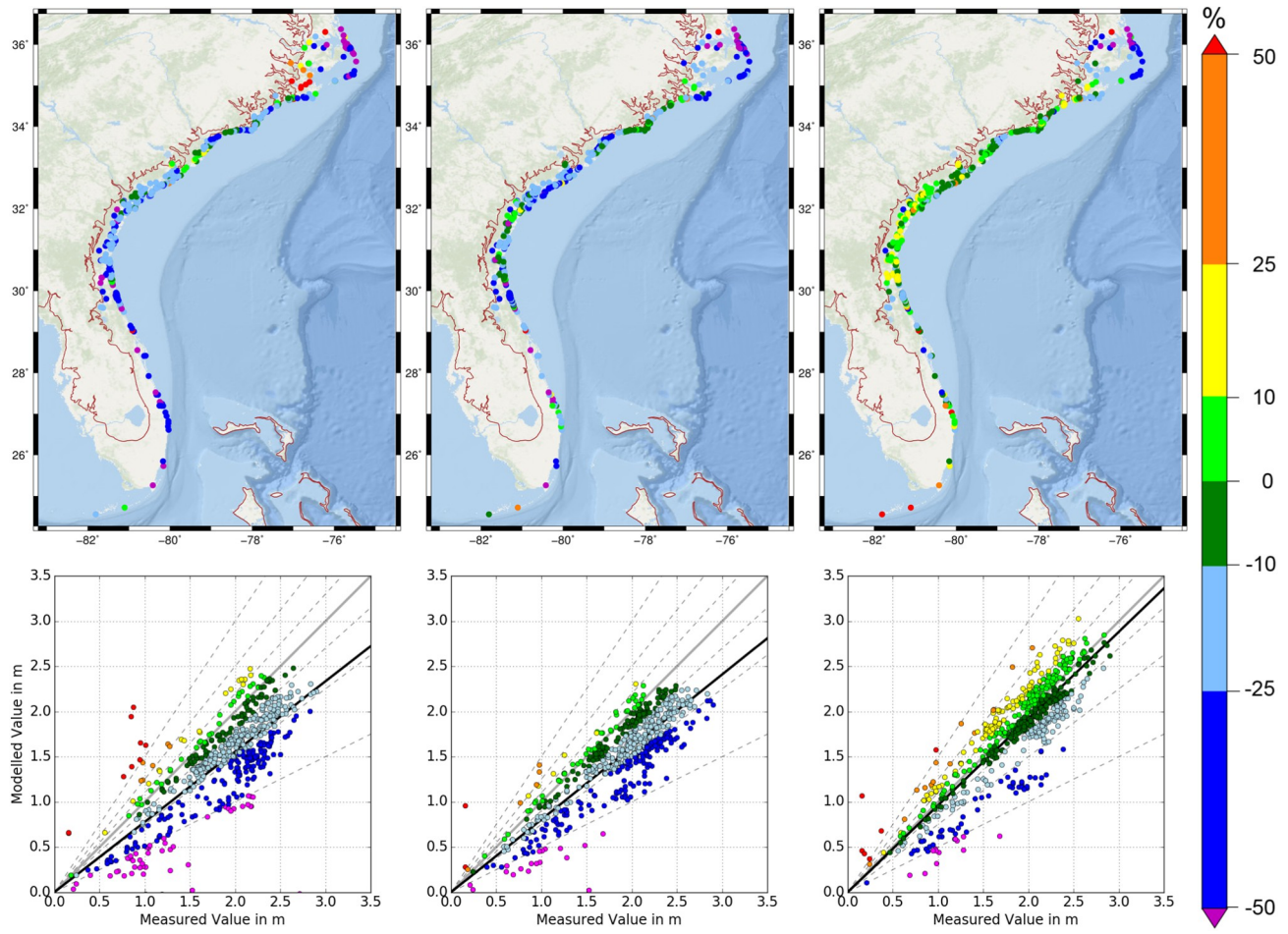

Fig. 10. Locations (top row) and scatter plots (bottom row) of HWMs and peak hydrograph values during Matthew. Columns correspond to: (left) GAHM; (center) WF; and (right) OWI. Colors indicate error expressed as a percentage of observed value. Green points indicate errors within 10%; yellow and light blue indicate errors between 10% and 25%; orange and dark blue indicate errors between 25% and 50%; and red and purple indicate errors over 50%. The thick gray and black lines represent $y = x$ and best-fit lines, respectively. Statistical metrics are shown in Table 2.

water levels along the open coastline (Fig. 14). The faster simulations produced larger water levels along the coastline as compared to the base Matthew simulation and the 50% slower scenario. About 260 km of coastline had water levels of 2 m or higher during Matthew. The 50% slower scenario caused a 6% decrease in this distance, whereas the 50% faster and 100% faster scenarios caused increases of 57% and 120%, respectively. Thus the faster storms would have pushed water levels of 2 m or higher against a longer stretch of coastline. But the inundation areas followed the opposite trends. Considering only the land regions that became wetted during the storm, Matthew had a total inundation volume of 5.5 km^3. For the 50% slower scenario, this volume was increased by 17%, while for the 50% and 100% faster scenarios, the volumes were decreased by about 6% and 16%, respectively. The faster storms increased the hazard at the open coast, while the slower storms pushed more flooding into overland regions. Thus although slower storms can produce more widespread flooding, faster storms can be dangerous as well, producing higher surges, especially at the coast.

Proudman (1953) showed that the largest storm surges occur when speed of the storm is close to the propagation speed of the long wave ($\sqrt{gh}$). For the 100% faster scenario, the storm forward speeds near the U.S. southeast coast were about 10 to 14 m/s which corresponds to a long wave for depths of 10 to 20 m. These isobaths vary in distances offshore along the U.S. southeast coast, but are within the region where the increased peaks were observed. Although the storm eye moved from south to north along the U.S. Atlantic coast, its anticlockwise winds caused the dominant direction of water velocities to be from north to south, with the coastline on its right side. Thus it is plausible that a faster storm would energize a shelf wave.

Increasing the forward speed of the storm caused an increase in peak water levels along the coastline but a decrease in overall volume of inundation. Regarding peak water levels, these results agree with Jelesnianski (1972) and Rego and Li (2009), whereas they contradict Peng et al. (2004) and Berg (2013). A slower storm causes lesser flooding on the open coast but pushes more water into the estuaries and bays. It also results in a larger total volume of inundation (Peng et al., 2004, 2006; Rego and Li, 2009). However, none of these studies looked at shore-parallel storm effects on a large extent of complex shoreline. Although Matthew had varying effects along the southeast U.S. coastline from Florida through North Carolina, the maximum water levels and overland flooding would have changed as expected if the storm's forward speed had been faster.

6. Conclusions

Matthew caused devastating floods, strong winds, and moderate storm surge along the southeast coast of the United States, and made landfall as a Category-2 hurricane along the central South Carolina coast during early October 2016. From east-central Florida to North Carolina, the storm moved slowly along a shore-parallel track and causing widespread impacts that lasted for several days. The SWAN + ADCIRC modeling system was used to perform high-resolution modeling of water levels during the storm, and predictions were

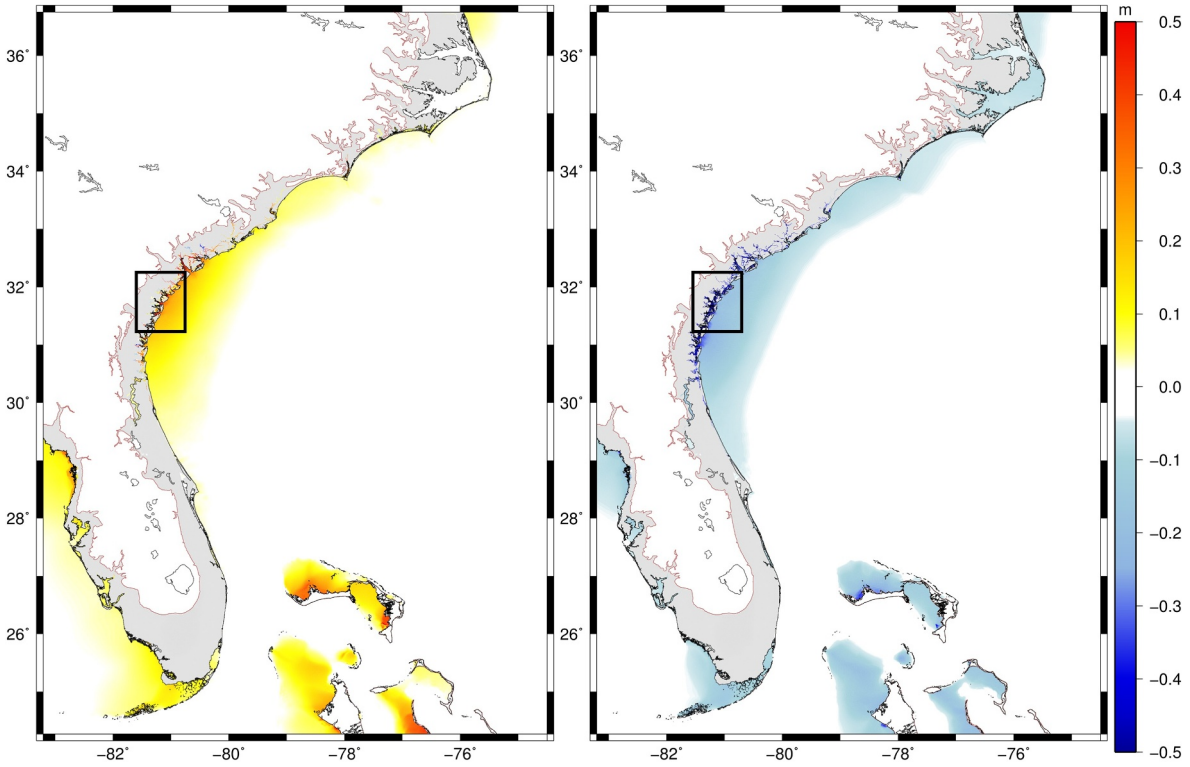

Fig. 11. Nonlinear interactions on the U.S. southeast coast during Matthew. Columns correspond to: (left) positive maximum values and (right) negative maximum values. OWI was used as the source of meteorological forcing for the simulations with only winds, and winds and tides together. Boxes indicate the location of the region shown in Fig. 12.

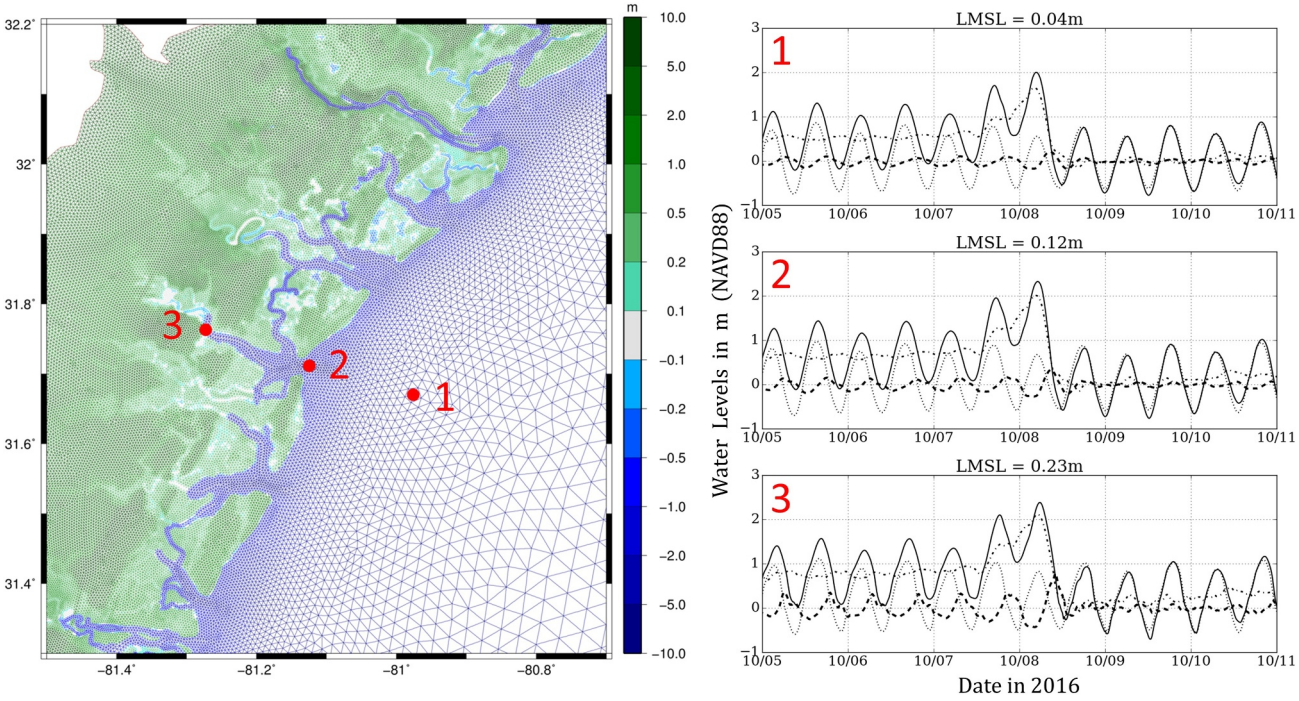

Fig. 12. Nonlinear interaction terms during Matthew at three locations along the Blackbeard Creek, south of Savannah, Georgia. Columns correspond to: (left) location of stations and (right) time-series of water levels (m relative to NAVD88) with line types corresponding to: (solid) total water levels, (dashed-dotted) surge only, (dotted) tides-only, and (dashed) nonlinear terms. OWI was used as the source of meteorological forcing for the simulations with only winds, and winds and tides together.

validated using the extensive network of observations throughout the region. Scenarios then quantified the effects of storm timing and forward speed on the surge and inundation. Our findings can be summarized as follows:

1. *Observation-based wind fields like WF and OWI provide better meteorological forcing for hindcasting, as compared to parametric models like GAHM.* This is evident from their lower values of E_{RMS} and B_{MN} for both surface pressure deficits and wind speeds. OWI had the lowest

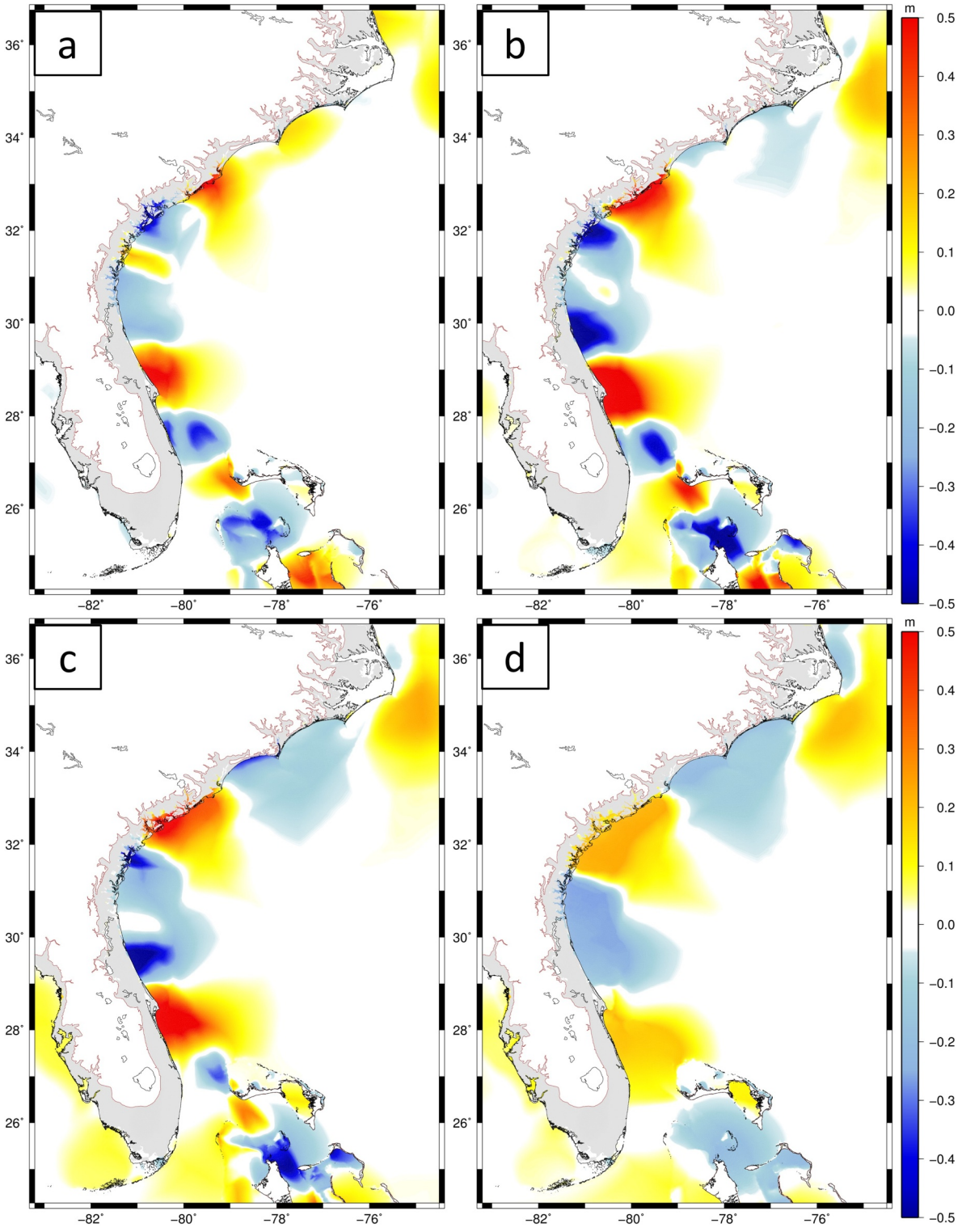

Fig. 13. Change in maximum water levels on delaying the storm by: (a) 3.11h; (b) 6.21h; (c) 9.32h; and (d) 12.42h. OWI was used as the source of wind forcing for all these simulations. The coastline is shown in black and the mesh boundary in brown.

error metrics, thus making it the most accurate wind and pressure fields during Matthew.

2. *SWAN + ADCIRC represents well the effects of Matthew along the U.S. Atlantic coast, even when applied on the relatively-coarse HSOFS mesh.* The model results using OWI forcing showed good agreement to observations for water levels and HWMs. Water level comparisons at 241 locations on the U.S. southeast coast resulted in an overall E_{RMS} of less than 30 cm and a B_{MN} very close to zero. There was also good correlation between modeled and measured peak water levels. For a total of 622 HWMs, the R^2 value was 0.78 and the slope of the best-fit line was 0.96. These values are comparable to results from studies using meshes with much higher resolution.
3. *The nonlinear interactions between tides and surge on the southeast U.S. Atlantic coast during Matthew had a constructive effect on the total water levels during a low or falling tide and a destructive effect during a high or rising tide.* This study is the first to consider these interactions

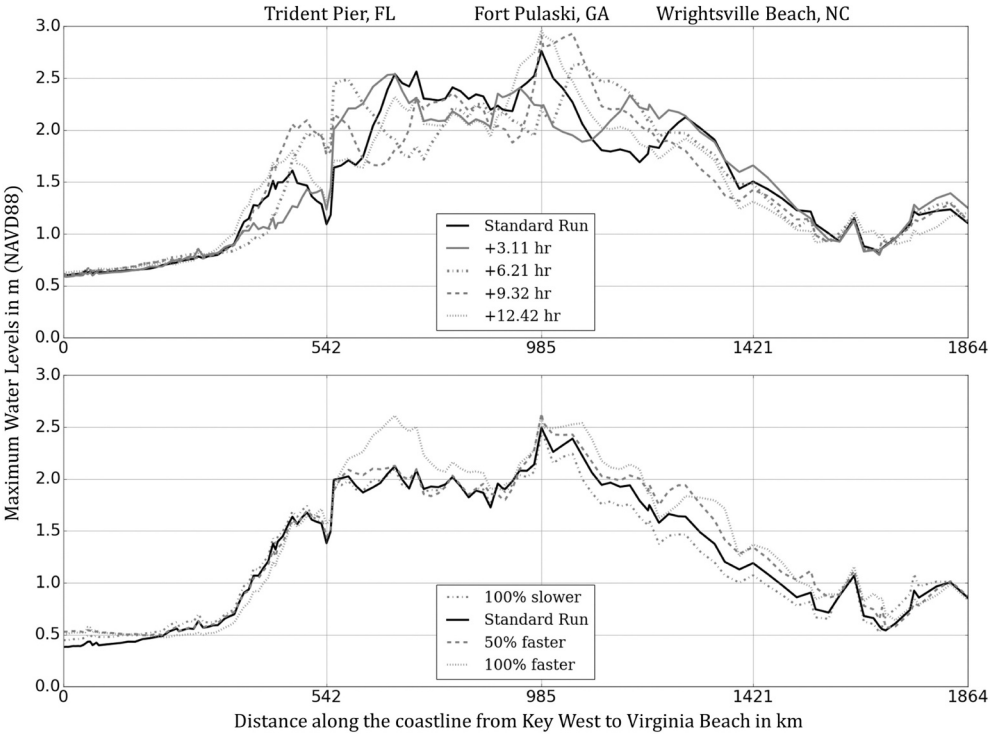

Fig. 14. Variation in maximum water levels along the coastline on altering the storm timing (top) and forward speed (bottom). Water levels during the standard Matthew run are indicated by black solid lines and those from perturbations are shown using gray color with line types (solid, dashed, dotted or dashed-dotted) as indicated in the figure legends. OWI was used as the source of wind forcing for all these simulations.

for a long coastline during a shore-parallel storm. The magnitudes of these interactions varied at different regions with respect to the coast, with small values on the ocean side and large values on the estuary side. In the estuaries, these interactions were larger than 1 m, larger than in previous studies.

4. *Altering the timing of the storm caused locations along the coast to have increased or decreased water levels depending on how the storm coincided with various stages in the tidal cycle.* This is especially true for shore-parallel storms that travel along a large extent of the coastline over several tidal cycles.
5. *The storm's forward speed also had large effects on water levels.* This study is the first to consider these interactions for a long coastline during a shore-parallel storm. Slower storms with more time to impact the coastal waters cause more flooding in the bays and estuaries, and lesser values on the open coast. Faster storms moving quickly across the coastline cause high surges on the open coast, especially along straight coastlines and lower surges in the bays and estuaries.

Although this study is specific to Hurricane Matthew, it demonstrates the importance of considering the nonlinear tide-surge interactions in flood risk studies. It also shows that storm timing and forward speed can be two crucial factors that can significantly alter the surge during a hurricane.

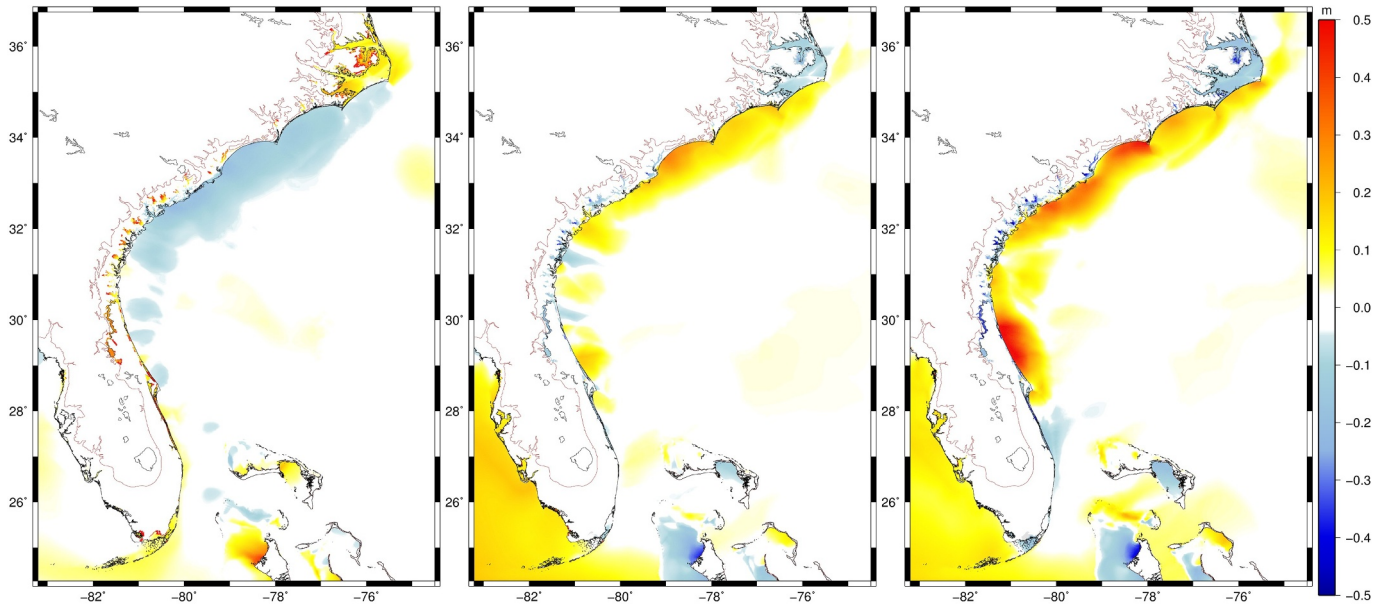

Fig. 15. Change in maximum water levels on changing the forward speed of the storm: (left) decreasing by 50%, (center) increasing by 50%, and (right) increasing by 100%. OWI was used as the source of wind forcing for all these simulations. The coastline is shown in black and the mesh boundary in brown.

Acknowledgments

This work was supported by the NSF grant ENH-1635784. This material is also based upon work supported by the U.S. Department of Homeland Security under Grant Award Number 2015-ST-061-ND0001-01. The views and conclusions contained in this document are those of the authors and should not be interpreted as necessarily representing the official policies, either expressed or implied, of the U.S. Department of Homeland Security.

References

Antonov, J.I., Levitus, S., Boyer, T.P., 2005. Thermosteric sea level rise, 1955–2003. Geophysical Research Letters 32, L12602.

Asher, T.G., Luettich, R.A., Fleming, J.G., 2019. Ocean Modelling Under revision.

Berg, N.J., 2013. On the Influence of Storm Parameters on Extreme Surge Events at the Dutch Coast. Master's thesis. Civil Engineering and Management. University of Twente.

Bernier, N.B., Thompson, K.R., 2007. Tide-surge interaction off the east coast of Canada and northeastern United States. Journal of Geophysical Research 112, C06008.

Bhaskaran, P.K., Nayak, S., Bonthu, S.R., Murthy, P.L.N., Sen, D., 2013. Performance and validation of a coupled parallel ADCIRC-SWAN model for THANE cyclone in the Bay of Bengal. Environmental Fluid Mechanics 13, 601–623.

Blanton, B.O., Luettich, R.A., Hanson, J.L., Vickery, P., Slover, K., Langan, T., 2012. North Carolina Floodplain Mapping Program, Coastal Flood Insurance Study: Production Simulations and Statistical Analyses. Renaissance Computing Institute.

Blanton, B.O., Vickery, P.J., 2008. North Carolina Coastal Flood Analysis System: Hurricane Parameter Development. Renaissance Computing Institute.

Booij, N., Ris, R.C., Holthuijsen, L.H., 1999. A third-generation wave model for coastal regions, Part I, model description and validation. Journal of Geophysical Research 104, 7649–7666.

Bretschneider, C.L., Krock, H.J., Nakazaki, E., Casciano, F.M., 1986. Roughness of Typical Hawaiian Terrain for Tsunami Runup Calculations: A Users Manual. University of Hawaii.

Bunya, S., Dietrich, J.C., Westerink, J.J., Ebersole, B.A., Smith, J.M., Atkinson, J.H., Jensen, R.E., Resio, D.T., Luettich, R.A., Dawson, C.N., Cardone, V.J., Cox, A.T., Powell, M.D., Westerink, H.J., Roberts, H.J., 2010. A high-resolution coupled riverine flow, tide, wind, wind wave and storm surge model for southern Louisiana and Mississippi: part I — model development and validation. Monthly Weather Review 138, 345–377.

Cardone, V.J., Cox, A.T., Greenwood, J.A., Thompson, E.F., 1994. Upgrade of Tropical Cyclone Surface Wind Field Model. U.S. Army Corps of Engineers.

Cyriac, R., Dietrich, J.C., Fleming, J.G., Blanton, B.O., Kaiser, C., Dawson, C.N., Luettich, R.A., 2018. Variability in coastal flooding predictions due to forecast errors during Hurricane Arthur (2014). Coastal Engineering 137, 59–78.

Dawson, C.N., Westerink, J.J., Feyen, J.C., Pothina, D., 2006. Continuous, discontinuous and coupled discontinuous-continuous Galerkin finite element methods for the shallow water equations. International Journal for Numerical Methods in Fluids 52, 63–88.

Dietrich, J.C., Dawson, C.N., Proft, J., Howard, M.T., Wells, G., Fleming, J.G., Luettich, R.A., Westerink, J.J., Cobell, Z., Vitse, M., 2013a. Real-time forecasting and visualization of hurricane waves and storm surge using SWAN + ADCIRC and FigureGen. In: Dawson, C.N., Gerritsen, M. (Eds.), Computational Challenges in the Geosciences, pp. 49–70.

Dietrich, J.C., Muhammad, A., Curcic, M., Fathi, A., Dawson, C.N., Chen, S.S., Luettich, R.A., 2018. Sensitivity of storm surge predictions to atmospheric forcing during Hurricane Isaac. Journal of Waterway, Port, Coastal and Ocean Engineering 144.

Dietrich, J.C., Tanaka, S., Westerink, J.J., Dawson, C.N., Luettich, R.A., Zijlema, M., Holthuijsen, L.H., Smith, J.M., Westerink, L.G., Westerink, H.J., 2012. Performance of the unstructured-mesh, SWAN + ADCIRC model in computing hurricane waves and surge. Journal of Scientific Computing 52, 468–497.

Dietrich, J.C., Westerink, J.J., Kennedy, A.B., Smith, J.M., Jensen, R.E., Zijlema, M., Holthuijsen, L.H., Dawson, C.N., Luettich, R.A., Powell, M.D., Cardone, V.J., Cox, A.T., Stone, G.W., Pourtaheri, H., Hope, M.E., Tanaka, S., Westerink, L.G., Westerink, H.J., Cobell, Z., 2011a. Hurricane Gustav (2008) waves and storm surge: hindcast, validation and synoptic analysis in southern Louisiana. Monthly Weather Review 139, 2488–2522.

Dietrich, J.C., Zijlema, M., Allier, P.E., Holthuijsen, L.H., Booij, N., Meixner, J.D., Proft, J.K., Dawson, C.N., Bender, C.J., Naimaster, A., Smith, J.M., Westerink, J.J., 2013b. Limiters for spectral propagation velocities in SWAN. Ocean Modelling 70, 85–102.

Dietrich, J.C., Zijlema, M., Westerink, J.J., Holthuijsen, L.H., Dawson, C.N., Luettich, R.A., Jensen, R.E., Smith, J.M., Stelling, G.S., Stone, G.W., 2011b. Modeling hurricane waves and storm surge using integrally-coupled, scalable computations. Coastal Engineering 58, 45–65.

Ezer, T., Atkinson, L.P., Corlett, W.B., Blanco, J.L., 2013. Gulf Stream-induced sea level rise and variability along the U.S. mid-Atlantic coast. Journal of Geophysical Research 118, 685–697.

Feng, X., Olabarrieta, M., Valle-Levinson, A., 2016. Storm-induced semidiurnal perturbations to surges on the US Eastern Seaboard. Continental Shelf Research 114, 54–71.

Florida Institute of Technology, 2018. https://www.fit.edu/. [Retrieved 10 March 2018].

Gao, J., Luettich, R.A., Fleming, J.G., 2017. Development and evaluation of a generalized asymmetric tropical cyclone vortex model in ADCIRC. In Preparation.

Garratt, J.R., 1977. Review of drag coefficients over oceans and continents. Monthly Weather Review 105, 915–929.

Hasselmann, S., Hasselmann, K., Allender, J.H., Barnett, T.P., 1985. Computations and parameterizations of the nonlinear energy transfer in a gravity wave spectrum, part II: parameterizations of the nonlinear transfer for application in wave models. Journal of Physical Oceanography 15, 1378–1391.

Ho, F.P., Myers, V.A., 1975. Joint probability method of tide frequency analysis applied to Apalachicola Bay and St. George Sound, Florida. National Oceanic and Atmospheric Administration.

Holland, R.W., 1980. An analytic model of the wind and pressure profiles in hurricanes. Monthly Weather Review 108, 1212–1218.

Hope, M.E., Westerink, J.J., Kennedy, A.B., Kerr, P.C., Dietrich, J.C., Dawson, C.N., Bender, C.J., Smith, J.M., Jensen, R.E., Zijlema, M., Holthuijsen, L.H., Luettich Jr, R.A., Powell, M.D., Cardone, V.J., Cox, A.T., Pourtaheri, H., Roberts, H.J., Atkinson, J.H., Tanaka, S., Westerink, H.J., Westerink, L.G., 2013. Hindcast and validation of Hurricane Ike (2008) waves, forerunner, and storm surge. Journal of Geophysical Research: Oceans 118, 4424–4460.

Horsburgh, K.J., Wilson, C., 2007. Tide-surge interaction and its role in the distribution of surge residuals in the North Sea. Journal of Geophysical Research 112, 1–13.

Hu, K., Chen, Q., Kimball, K.S., 2012. Consistency in hurricane surface wind forecasting: an improved parametric model. Natural Hazards 61, 1029–1050.

Hu, K., Chen, Q., Wang, H., 2015. A numerical study of vegetation impact on reducing storm surge by wetlands in a semi-enclosed estuary. Coastal Engineering 95, 66–76.

Idier, D., Dumas, F., Muller, H., 2012. Tide-surge interaction in the English Channel. Natural Hazards and Earth System Sciences 12, 3709–3718.

Irish, J.L., Resio, D.T., Ratcliff, J.J., 2008. The influence of storm size on hurricane surge. Journal of Physical Oceanography 38, 2003–2013.

Jelesnianski, C.P., 1972. SPLASH: Special Program to List Amplitudes of Surges from Hurricanes. U.S. Dep. of Commer., Natl. Oceanic and Atmos. Admin., Natl. Weather Serv., Silver Spring, Maryland.

Kerr, P.C., Donahue, A.S., Westerink, J.J., Luettich, R.A., Zheng, L.Y., Weisburg, R.H., Huang, Y., Wang, H.V., Teng, Y., Forrest, D.R., Roland, A., Haase, A.T., Kramer, A.W., Taylor, A.A., Rhome, J.R., Feyen, J.C., Signell, R.P., Hanson, J.L., Hope, M.E., Estes, R.M., Dominguez, R.A., Dunbar, R.P., Semeraro, L.N., Westerink, H.J., Kennedy, A.B., Smith, J.M., Powell, M.D., Cardone, V.J., Cox, A.T., 2013. U.S. IOOS coastal and ocean modeling testbed: inter-model evaluation of tides, waves, and hurricane surge in the Gulf of Mexico. Journal of Geophysical Research: Oceans 118, 5129–5172.

Kinnmark, I., 1986. The shallow water wave equations: formulation, analysis and application. In: Brebbia, C.A., Orszag, S.A. (Eds.), Lecture Notes in Engineering. 15. Springer-Verlag, pp. 12–26.

Kolar, R.L., Westerink, J.J., Cantekin, M.E., Blain, C.A., 1994. Aspects of nonlinear simulations using shallow water models based on the wave continuity equations. Computers and Fluids 23, 1–24.

Levitus, S., Antonov, J.I., Boyer, T.P., Stephens, C., 2000. Warming of the world ocean. Science 287, 2225–2229.

Lin, N., Emmanuel, K., Oppenheimer, M., Vanmarcke, E., 2012. Physically based assessment of hurricane surge threat under climate change. Nature Climate Change 2, 462–467.

Luettich, R. A., Westerink, J. J., 2004. Formulation and numerical implementation of the 2D/3D ADCIRC finite element model version 44.XX. http://adcirc.org/adcirc_theory_2004_12_08.pdf.

Luettich, R.A., Westerink, J.J., Scheffner, N.W., 1992. ADCIRC: an advanced three-dimensional circulation model for shelves coasts and estuaries, report 1: theory and methodology of ADCIRC-2DDI and ADCIRC- 3DL. United States Army Corps of Engineers.

Madsen, O.S., Poon, Y.K., Graber, H.C., 1988. Spectral wave attenuation by bottom friction: theory. In: Proceedings 21st International Conference on Coastal Engineering, pp. 492–504.

Mattocks, C., Forbes, C., 2008. A real-time, event-triggered storm surge forecasting system for the state of North Carolina. Ocean Modelling 25, 95–119.

Mattocks, C., Forbes, C., Ran, L., 2006. Design and implementation of a real-time storm surge and flood forecasting capability for the state of North Carolina. University of North Carolina.

National Oceanic and Atmospheric Administration, 2017. National Data Buoy Center. http://www.ndbc.noaa.gov.

National Oceanic and Atmospheric Administration, 2018c. National Estuarine Research Reserve System. http://cdmo.baruch.sc.edu/. [Retrieved 10 March 2018].

National Oceanic and Atmospheric Administration, 2018b. National Ocean Service. https://oceanservice.noaa.gov/. [Retrieved 10 March 2018].

National Oceanic and Atmospheric Administration, 2018d. NOAA's Integrated Coral Observing Network. http://ecoforecast.coral.noaa.gov/. [Retrieved 10 March 2018].

National Oceanic and Atmospheric Administration, 2018a. Sea Level Trends. https://tidesandcurrents.noaa.gov/sltrends/sltrends.html. [Retrieved 09 March 2018].

National Park Service, 2018. NPS's Everglades National Park. http://ecoforecast.coral.noaa.gov/. [Retrieved 10 March 2018].

Niedoroda, A.W., Resio, D.T., Toro, G., Divoky, D., Reed, C., 2010. Analysis of the coastal Mississippi storm surge hazard. Ocean Engineering 37, 82–90.

North Carolina Emergency Management, 2018. Flood Inundation Mapping and Alert Network. https://fiman.nc.gov/. [Retrieved 10 March 2017].

Peng, M., Xie, L., Pietrafesa, L.J., 2004. A numerical study of storm surge and inundation in the Croatan-Albemarle-Pamlico estuary system. Estuarine, Coastal and Shelf Science 59, 121–137.

Peng, M., Xie, L., Pietrafesa, L.J., 2006. A numerical study on hurricane-induced storm surge and inundation in Charleston Harbor, South Carolina. Journal of Geophysical Research 111, 81–101.

Poulose, J., Rao, A.D., Bhaskaran, P.K., 2017. Role of continental shelf on non-linear

interaction of storm surges, tides and waves: an idealized study representing the west coast of India. Estuarine, Coastal and Shelf Science 1–14.
Prandle, D., Wolf, J., 1978. Surge-tide interaction in the Southern North Sea. Hydrodynamics of Estuaries and Fjords 23, 161–185.
Proudman, J., 1953. Dynamical Oceanography. John Wiley and Sons, New York, pp. 409.
Proudman, J., 1955. The propagation of tide and surge in an estuary. In: Proceedings of the Royal Society of London. A231. pp. 8–24.
Proudman, J., 1957. Oscillations of tide and surge in an estuary of finite length. Journal of Fluid Mechanics 2, 371–382.
Rego, J.L., Li, C., 2009. On the importance of the forward speed of hurricanes in storm surge forecasting: a numerical study. Geophysical Research Letters 36, L07609.
Rego, J.L., Li, C., 2010. Nonlinear terms in storm surge predictions: effect of tide and shelf geometry with case study from Hurricane Rita. Journal of Geophysical Research 115, C06020.
Technology, Riverside, AECOM, 2015. Mesh development, tidal validation, and hindcast skill assessment of an ADCIRC model for the Hurricane Storm Surge Operational Forecast System on the US Gulf-Atlantic Coast.
Rossiter, J.R., 1961. Interaction between tide and surge in the Thames. Geophysical Journal of the Royal Astronomical Society 6, 29–53.
Schloemer, R.W., 1954. Analysis and synthesis of hurricane wind patterns over Lake Okechobee, FL. Govt. Printing Office.
Scripps Institution of Oceanography, 2018. The Coastal Data Information Program. http://cdip.ucsd.edu/. [Retrieved 10 March 2018].
Sebastian, A.G., Proft, J.M., Dietrich, J.C., Du, W., Bedient, P.B., Dawson, C.N., 2014. Characterizing hurricane storm surge behavior in Galveston Bay using the SWAN + ADCIRC model. Coastal Engineering 88, 171–181.
Skamarock, W.C., Klemp, J.B., Dudjia, J., Gill, D.O., Barker, D.M., Duda, M.G., Huang, X.Y., Wang, W., Powers, J.G., 2008. A description of the Advanced Research WRF Version 3. NCAR.
Stewart, S.R., 2017. Tropical Cyclone Report for Hurricane Matthew. National Hurricane Center.
Suh, S.W., Lee, H.Y., Kim, H.J., Fleming, J.G., 2015. An efficient early warning system for typhoon storm surge based on time-varying advisories by coupled ADCIRC and SWAN. Ocean Dynamics 65, 617–646.
Szpilka, C., Dresback, K., Kolar, R., Feyen, J., Wang, J., 2016. Improvements for the Western North Atlantic, Caribbean and Gulf of Mexico ADCIRC tidal database (EC2015). Journal of Marine Science and Engineering 4, 72.
Tanaka, S., Bunya, S., Westerink, J.J., Dawson, C.N., Luettich, R.A., 2011. Scalability of an unstructured grid continuous Galerkin based hurricane storm surge model. Journal of Scientific Computing 46, 329–358.
Tang, Y.M., Grimshaw, R., Sanderson, B., Holland, G., 1996. A numerical study of storm surges and tides, with application to the North Queensland coast. Journal of Physical Oceanography 26, 2700–2711.
Thompson, E.F., Cardone, V.J., 1996. Practical modeling of hurricane surface wind fields. Journal of Waterway, Port, Coastal, and Ocean Engineering 122, 195–205.
University of North Carolina, 2018. Coastal Studies Institute. http://coastalstudiesinstitute.org/. [Retrieved 10 March 2018].
University of North Carolina Wilmington, 2018. Coastal Ocean Research and Monitoring Program. http://cormp.org/. [Retrieved 10 March 2018].
U.S. Army Corps of Engineers, 2018a. http://www.usace.army.mil/. [Retrieved 10 March 2018].
U.S. Army Corps of Engineers, 2018b. North Atlantic Coast Comprehensive Study report. http://www.nad.usace.army.mil/CompStudy/. [Retrieved 13 March 2018].
U.S. Geological Survey, 2018a. Elevation. https://nationalmap.gov/elevation.html. [Retrieved 09 March 2018].
U.S. Geological Survey, 2018b. USGS Current Water for the Nation. https://waterdata.usgs.gov/nwis/rt. [Retrieved 10 March 2018].
U.S. Geological Survey, 2018c. USGS Flood Event Viewer. https://water.usgs.gov/floods/FEV/. [Retrieved 10 March 2018].
Valle-Levinson, A., Olabarrieta, M., Valle, A., 2013. Semidiurnal perturbations to the surge of Hurricane Sandy. Geophysical Research Letters 40, 2211–2217.
Weisburg, R.H., Zheng, L., 2006. Hurricane storm surge simulations for Tampa Bay. Estuaries and Coasts 29, 899–913.
Westerink, J.J., Luettich Jr, R.A., Feyen, J.C., Atkinson, J.H., Dawson, C.N., Roberts, H.J., Powell, M.D., Dunion, J.P., Kubatko, E.J., Pourtaheri, H., 2008. A basin to channel scale unstructured grid hurricane storm surge model applied to southern Louisiana. Monthly Weather Review 136, 833–864.
Willis, J.K., Roemmich, D., Cornuelle, B., 2004. Interannual variability in upper ocean heat content, temperature,and thermosteric expansion on global scales. Journal of Geophysical Research 109, C12036.
Wolf, J., 1978. Interaction of tide and surge in a semi-infinite uniform channel, with application to surge propagation down the east coast of Britain. Applied Mathematical Modeling 2, 245–253.
Wolf, J., 1981. Surge-tide interaction in the North Sea and River Thames. Floods due to High Winds and Tides 75–94.
Xie, L., Bao, S., Pietrafesa, L.J., Foley, K., Fuentes, M., 2006. A real-time hurricane surface wind forecasting model: formulation and verification. Monthly Weather Review 134, 1355–1370.
Zhang, W., Shi, F., Hong, H., Shang, S., Kirby, J.T., 2010. Tide-surge interaction intensified by the Taiwan Strait. Journal of Geophysical Research 115, C06012.
Zijlema, M., 2010. Computation of wind-wave spectra in coastal waters with SWAN on unstructured grids. Coastal Engineering 57, 267–277.